Check for updates

The surface topography of silicone breast implants mediates the foreign body response in mice, rabbits and humans

Joshua C. Doloff [1,2,3,4,5,22] ✉, Omid Veiseh [1,2,3,6,22] ✉, Roberto de Mezerville [7] ✉, Marcos Sforza[8], Tracy Ann Perry[7], Jennifer Haupt[9], Morgan Jamiel[9], Courtney Chambers[10], Amanda Nash[6], Samira Aghlara-Fotovat[6], Jessica L. Stelzel [4], Stuart J. Bauer[4], Sarah Y. Neshat [4], John Hancock[7], Natalia Araujo Romero[7], Yessica Elizondo Hidalgo[7], Isaac Mora Leiva[7], Alexandre Mendonça Munhoz[11,12], Ardeshir Bayat[13], Brian M. Kinney[14], H. Courtney Hodges [6,15,16,17], Roberto N. Miranda [18], Mark W. Clemens[19] and Robert Langer [1,2,3,20,21] ✉

Silicone is widely used in chronic implants and is generally perceived to be safe. However, textured breast implants have been associated with immune-related complications, including malignancies. Here, by examining for up to one year the foreign body response and capsular fibrosis triggered by miniaturized or full-scale clinically approved breast implants with different surface topography (average roughness, 0–90 μm) placed in the mammary fat pads of mice or rabbits, respectively, we show that surface topography mediates immune responses to the implants. We also show that the surface surrounding human breast implants collected during revision surgeries also differentially alters the individual's immune responses to the implant. Moreover, miniaturized implants with an average roughness of 4 μm can largely suppress the foreign body response and fibrosis (but not in T-cell-deficient mice), and that tissue surrounding these implants displayed higher levels of immunosuppressive FOXP3+ regulatory T cells. Our findings suggest that, amongst the topographies investigated, implants with an average roughness of 4 μm provoke the least amount of inflammation and foreign body response.

Poly(dimethylsiloxane) (PDMS) is one of the most widely used polymers in the fabrication of medical devices developed for chronic (long-term) implantation into the body[1]. Many clinically approved tissue-contacting artificial devices, including intraocular lenses[2], dialysis membranes[3], finger joints[4], ventriculoperitoneal shunt systems[5] and devices for plastic and reconstructive surgery[6], use a silicone elastomer, such as PDMS, as their platform material. The favourable material properties of PDMS, such as high oxygen permeability and tunable stiffness, and the initial perception of its biological inertness, have rendered it an attractive choice for the medical device industry[7]. However, over time it has become apparent that PDMS-based devices can provoke unpredictable immune responses and excessive foreign body reactions in many individuals[8–10].

For example, a majority of the 400,000 women in the United States who receive silicone breast implants every year for cosmetic or reconstructive reasons will require replacement within 10 to 20 years due to capsular contracture, which is induced by excessive foreign body response (FBR) to the implant (https://www.fda.gov/consumers/consumer-updates/what-know-about-breast-implants). These immune-driven fibrotic responses can lead to pain and discomfort for the individual as well as device failure[10,11].

To alleviate immune responses to PDMS implants, different approaches have been evaluated, including chemical modification to alter surface chemistry[12], coating with hydrogels[13], plasma treatment[14] and altering surface features such as topography and roughness[15]. Among these strategies, the alterations in surface

[1]David H. Koch Institute for Integrative Cancer Research, Massachusetts Institute of Technology, Cambridge, MA, USA. [2]Department of Chemical Engineering, Massachusetts Institute of Technology, Cambridge, MA, USA. [3]Department of Surgery, Boston Children's Hospital, Harvard Medical School, Boston, MA, USA. [4]Department of Biomedical Engineering, Translational Tissue Engineering Center, Wilmer Eye Institute, Johns Hopkins University School of Medicine, Baltimore, MD, USA. [5]Department of Materials Science and Engineering, Institute for NanoBioTechnology, Johns Hopkins University, Baltimore, MD, USA. [6]Department of Bioengineering, Rice University, Houston, TX, USA. [7]Establishment Labs Holdings, Alajuela, Costa Rica. [8]Division of Plastic Surgery, Dolan Park Hospital, Birmingham, UK. [9]Division of Comparative Medicine, Massachusetts Institute of Technology, Cambridge, MA, USA. [10]Translational Biology and Molecular Medicine Graduate Program, Baylor College of Medicine, Houston, TX, USA. [11]Breast Surgery Group, Plastic Surgery Division, University of São Paulo School of Medicine, São Paulo, Brazil. [12]Plastic Surgery Department, Hospitals Sirio-Libanês and Moriah, São Paulo, Brazil. [13]Plastic and Reconstructive Surgery Research, NIHR Biomedical Research Centre, University of Manchester, Manchester, UK. [14]Division of Plastic Surgery, Keck School of Medicine, University of Southern California, Los Angeles, CA, USA. [15]Department of Molecular and Cellular Biology, Baylor College of Medicine, Houston, TX, USA. [16]Center for Cancer Epigenetics, The University of Texas MD Anderson Cancer Center, Houston, TX, USA. [17]Center for Precision Environmental Health, Baylor College of Medicine, Houston, TX, USA. [18]Department of Hematopathology, Division of Pathology/Lab Medicine, The University of Texas MD Anderson Cancer Center, Houston, TX, USA. [19]Department of Plastic Surgery, University of Texas, MD Anderson Cancer Center, Houston, TX, USA. [20]Harvard-MIT Division of Health Science Technology, Massachusetts Institute of Technology, Cambridge, MA, USA. [21]Institute for Medical Engineering and Science, Massachusetts Institute of Technology, Cambridge, MA, USA. [22]These authors contributed equally: Joshua C. Doloff, Omid Veiseh. ✉e-mail: jcdoloff@jhu.edu; omid.veiseh@rice.edu; rdemezerville@establishmentlabs.com; rlanger@mit.edu

architecture have been most widely explored in the clinic to influence immune responses and fibrosis[15–17]. In particular, a number of commercially marketed silicone-based breast implant products are offered with surfaces ranging from smooth to macrotextured[16]. To stratify the different breast implant surfaces, a classification system was recently reported[17,18]. The International Organization for Standardization (ISO) 14607:2018 (Non-active surgical implants—Mammary implants—Particular requirements) offers a classification system based on surface topography, for which surfaces are imaged by scanning electron microscopy (SEM) and surface roughness (Ra) measurements are determined by optical, contact or non-contact profilometry[18]. According to the ISO classification, and on the basis of Ra measurements, breast implant surfaces are designated as smooth (Ra < 10 μm), microtextured (10 μm ≤ Ra ≤ 50 μm) or macrotextured[19] (Ra > 50 μm) (Supplementary Table 1). Clinical studies suggest that these different surface architectures produce different foreign body immune responses and fibrosis[20,21]. Of note, breast implant-associated anaplastic large cell lymphoma (BIA-ALCL), a cancer of immune T cells, has only been observed in response to textured surface implants, and not to the traditionally used smooth surface implants[22,23]. It has been postulated that textured surfaces limit capsular contracture (a problem historically associated with smooth implants) by inducing a different immune reaction that discourages formation of fibrous tissue around the breast implant after implantation[12] (Supplementary Table 2a). It has also been reported that macrotextured implants induce an excessive inflammatory response and chronic antigenic stimulation[24]. Such persistent inflammation can produce deleterious effects such as pain, fluid accumulation, infection and, in rare cases, lymphoma[16]. In 2019, the US Food and Drug Administration requested a class I device recall of textured breast implants and tissue expanders from one US manufacturer because the devices were associated with an elevated risk for developing BIA-ALCL compared with smooth devices[25]. Higher incidences of BIA-ALCL correlated with individuals who received aggressively textured breast implants with surface roughness greater than 300 μm compared with smooth versions[26]. In contrast to smooth surface implants, textured surfaces release particulate debris which is digested by macrophages, leading to perpetual exhaustive phagocytosis, inflammatory cytokine release and lymphocyte proliferation[27,28]. A tribology hypothesis represents another possible aetiology of BIA-ALCL in which mechanical shear stress may trigger an overt inflammatory response, potentially contributing to the formation of double capsules[29].

Silicone implants induce a specific local immune reaction, which is orchestrated by macrophage adhesion and spreading mediated by interleukin-1 (IL-1) production, activation of T helper 1 (T_H1) and T_H17 cells, and myofibroblast activation that results in fibrosis[7,30,31]. At the cellular level, surface roughness can influence cell adhesion, spreading, migration, proliferation and differentiation into various cell types[23,32–34]. For example, it has been demonstrated that adhered macrophages that were spatially restricted by surface architectures led to reduced inflammatory responses[33]. Another group demonstrated that biomimetic silicone surfaces with hierarchical micro- and nano-topographical features of 2–5 μm facilitated improved spreading of breast fibroblasts and reduced inflammatory responses

compared with cells grown on completely smooth or larger macrotextured surfaces (Ra > 50 μm)[35]. However, the kinetics and composition of immune responses are not fully understood, and it remains unclear which surface design is optimal for improving biocompatibility[21]. Currently, clinicians and regulatory agencies are challenged with advising patients on how to best manage risk of immune complications due to limited scientific data in the literature (https://www.fda.gov/regulatory-information/search-fda-guidance-documents/breast-implants-certain-labeling-recommendations-improve-patient-communication). Furthermore, the US Food and Drug Administration has not yet cleared any devices (that is, surface treatments whether modified chemistry or physical architecture) to treat or reduce fibrous capsular contracture of breast implants (https://www.fda.gov/medical-devices/breast-implants/risks-and-complications-breast-implants). Therefore, a careful systemic investigation is needed to explain the mechanism for altered immune responses through modification of surface texture.

Here, we report the findings of studies that we carried out to systematically understand immune responses to six commercial breast implants with varied surface topographies: traditional Smooth (Mentor Smooth Round) controls, SmoothSilk/SilkSurface (Motiva), microtextured VelvetSurface (Motiva), microtexured Siltex Round (Mentor MemoryGel), microtextured Microcell (Allergan) and macrotextured Biocell Round (Allergan NATRELLE INSPIRA SoftTouch). These breast implants produce varying foreign body reactions and fibrosis complications in human recipients (https://www.fda.gov/media/80685/download; Supplementary Table 2a). Of note among these products, SmoothSilk, also known as SilkSurface, bioengineered by Motiva and Establishment Labs, has shown a low rate of overall complications to date in a recent short-term clinical follow-up study[36]. To further explain the mechanisms associated with varying degrees of fibrosis as a function of surface architecture, we explored a hypothesis that the SmoothSilk surface could alter the kinetics and composition of foreign body reactions to enable long-term device function in the absence of substantial inflammation and fibrous encapsulation. Long-term anti-fibrotic efficacy was observed across two different animal models—up to 1 year in New Zealand White rabbits bearing subcutaneous human-sized, commercial implants, as well as up to 6 months in C57BL/6 mice with a range of miniaturized implant mimics engineered by different manufacturing processes similar to those used for their full-scale commercial counterparts. Mechanistic studies performed using wild-type and T-cell-deficient (nude) C57BL/6 mice, which have previously been used as a model system for fibrosis[37–39], demonstrated significantly decreased levels of macrophages only in wild-type tissue immediately surrounding SmoothSilk implants. The immune responses in the animals were validated by comparing them to human clinical specimens across representative implant surfaces. Clinical specimens were taken from the luminal surface of long-term (range 7 months to 11 years) breast implant scar capsules for both cosmetic augmentation and breast cancer reconstruction revisionary surgery. Macrophages are known key mediators of the immune response to implanted biomaterials and the digestion of shed particulate debris[37,40,41], and complicate long-term fibrosis suppression due to constant

Fig. 1 | Roughness and chemical composition of human-scale implants versus miniaturized implant mimics. a, SEM images of human-scale (100–220 cm³) breast implants, used in rabbits (as described in Fig. 2) versus miniaturized breast implants used in pro-fibrotic C57BL/6 mice (Figs. 3–5). SEM analysis confirmed that miniaturized implants have a similar range of surface topographies for potential modulation of capsular contraction and host rejection. PU, polyurethane. **b**, Profilometry images showing peak intensity (kurtosis) and surface uniformity (skewness). **c,d**, Quantification of implant shell surface topographies as measured by profilometry for both human-sized (**c**) and miniaturized (**d**) implants. Commercial names are used for the human implants whereas mean surface roughness (topography) values are used to describe the miniaturized implant mimics. **e,f**, XPS analysis was performed on the shell surfaces of commercial human breast implants (**e**) and miniaturized implant mimics (**f**). Platinum was not detectable (ND) in any of the implant shells. In bar graphs, data are mean ± s.d. of technical replicates.

replenishment in the body[42]. Importantly, increases in local regulatory T cell levels were also observed immediately around the margins of implants with increased roughness, but capsular thickness and FBR was only suppressed when roughness was specifically finely tuned to be single-cell scale (that is, of a similar scale to immune lymphocytes)[35,43].
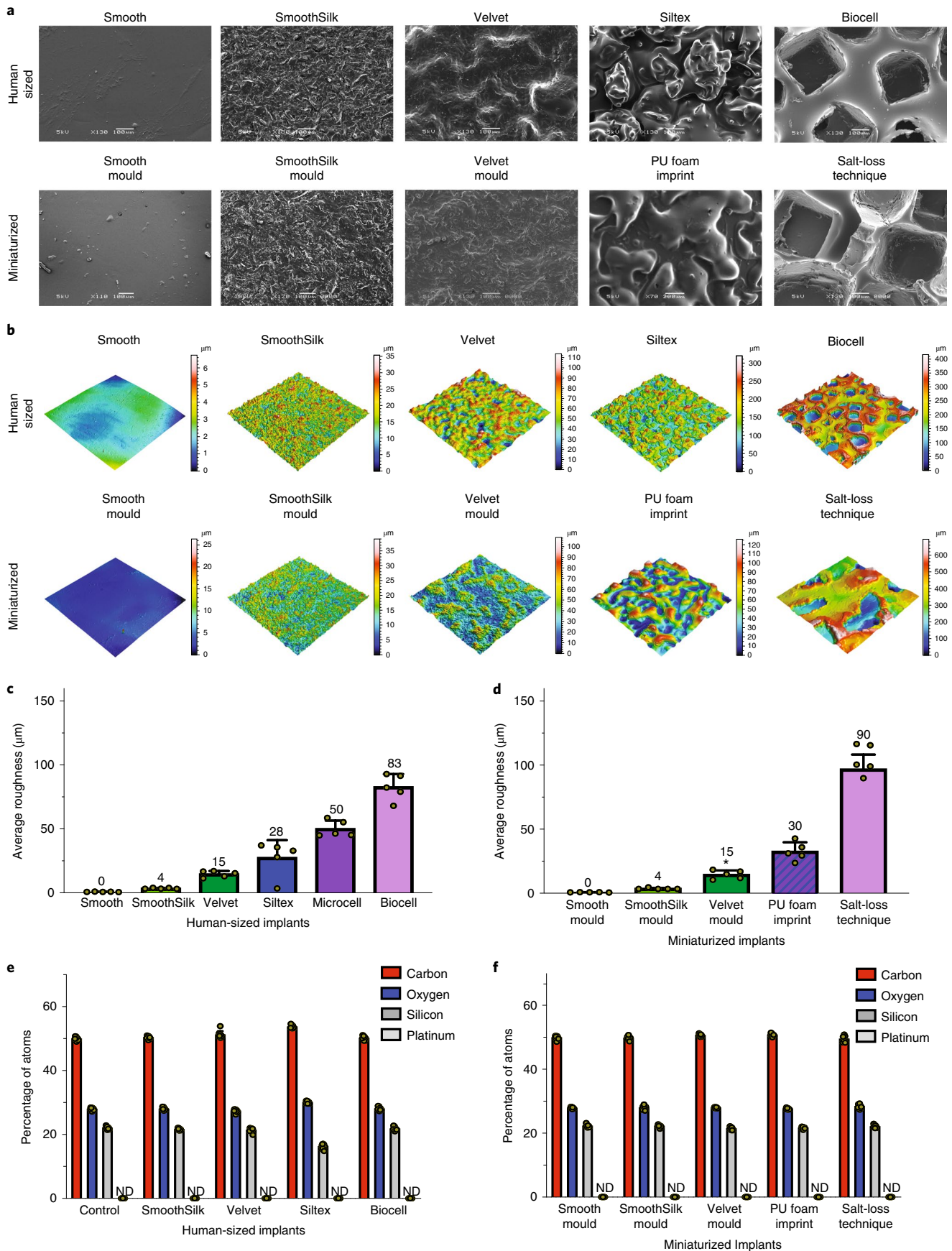
Results

Implant surface characterization of commercial and miniaturized implants. We sought to study the immune profile of silicone breast implants as a function of surface topography ranging from smooth to macrotextured. To do so, we first characterized the surface properties of five US and/or EU regulatory agency-approved, full-scale commercial breast implant products to quantify and contrast differential surface features (Fig. 1 and Supplementary Fig. 1). First, SEM was used to image each implant surface (Fig. 1a). Non-contact profilometry was then used to quantify breast implant average peak surface roughness (Ra) and additional surface features (that is, variations in the height of the surface relative to a reference plane) for all implant groups (Fig. 1b and Supplementary Fig. 1a,b). Implant surface skewness, a measure for prominence of surface peaks versus valleys—with positive skewness corresponding to more peaks than valleys and negative skewness corresponding to more valleys than peaks (Supplementary Fig. 1a)—was quantified in each case (Supplementary Fig. 1b). To help understand how implant surface features may affect surrounding tissues at the interaction interface with implant surfaces, we measured static and dynamic friction coefficients, as measures of shear force application needed to start or maintain active implant movement at a constant velocity against the tissue (Supplementary Fig. 1c). In addition, to help understand how different surface features collectively map across implant types, we created a spiderweb plot in which implant surface area, kurtosis (measure of sharpness, or lack thereof, of peak size distribution or dispersity), density of peaks and roughness were all simultaneously considered (Supplementary Fig. 1d). Finally, we performed X-ray photoelectron spectroscopy (XPS) on outer implant shells to monitor for any differences in surface chemistry (Fig. 1e,f). Overall, with the exception of Siltex, which had very minor single-digit deviations, elemental analysis across all implants ($n = 5$ per group) showed no statistically significant differences in abundance of carbon, oxygen or silicone. To ensure that implant response would not be affected by any residual catalyst remaining following manufacturing, we also confirmed a lack of detectable platinum levels in any of the implant shells.

To further examine the hypothesis that surface features can affect foreign body immune responses we also generated miniaturized implants for subsequent implantation testing in mice. Each miniaturized implant shell was produced using similar manufacturing practices to their clinical implant counterparts (Methods). Specifically, mould-cast shells were used for control Smooth, SmoothSilk and VelvetSurface implants, polyurethane foam imprinting was used for comparison to Siltex, and salt-loss manufacturing was used for production of a miniaturized implant system comparable to Microcell and Biocell implants (Fig. 1 and Supplementary Fig. 2a). As with the clinical implants, SEM was used to image each mouse-scale implant (0, 4, 15, 30 and 90 μm in size) surface for direct comparison (Fig. 1a, top versus bottom). Profilometry was used as well as a quantitative measure of surface topography (Fig. 1b and Supplementary

Fig. 2a), and showed similar representative values between clinical and mouse implants (Fig. 1c versus Fig. 1d). Further, as indicated across all full-scale implant groups, XPS on outer miniaturized implant shells confirmed no significant differences in surface chemistry across implant groups (Fig. 1e,f and Supplementary Fig. 2b).

Implant topography mediates host immune response leading to suppression of FBR. Next, to characterize tissue response, we implanted the 6 size-matched (180–205 cm³) commercially available silicone breast implants with a range of surface topographies (traditional Smooth (Mentor), SmoothSilk (Motiva), VelvetSurface (Motiva), Siltex (Mentor), Microcell (Allergan) and Biocell (Allergan); $n = 5$ per group) subcutaneously with full sterile technique including insertion sleeves (but without soaking implants in betadine, due to reported effects of cellular toxicity and contraindication from the manufacturers) into naive (no prior procedures or treatments), weight-matched (3.2–4 kg) female New Zealand White rabbits for both a shorter 3 week as well as a long-term 6 month period (Fig. 2 and Supplementary Fig. 3). After each incubation period, implants were retrieved and analysed for the presence of encapsulation and potential contracture, viewed as ripples or tension lines in the outer skin and capsule (Fig. 2a,b, Supplementary Figs. 4–7 and Supplementary Table 2b). While all topography ranges resulted in a capsule, SmoothSilk elicited the thinnest capsule, which had an almost translucent appearance, suggesting differential modulation of host immune cells. In addition, SmoothSilk and VelvetSurface implants demonstrated little to no capsular tension lines and rippling or folding compared with traditional Smooth control, Siltex, Microcell and Biocell implants (Supplementary Figs. 4 and 6 and Supplementary Table 2b). These observations were consistent across both 3 week as well as 6 month time points (Supplementary Table 2b). Furthermore, Siltex, Microcell and Biocell implants all showed double capsule formation (Fig. 2b–d and Supplementary Figs. 4–8), a commonly observed phenomenon in the clinic in human recipients with higher-roughness surfaces[29,44,45], which we observed as early as 3 weeks after implantation and still present on 6 month retrievals. All inner capsules appeared to be thinner than outer capsules, and had a denser and plastic-like white deposition matrix (Fig. 2a–d, yellow dashed lines and Supplementary Figs. 4c–e, 5, 6d–f and 8), as opposed to softer and less dense outer capsules (Fig. 2c,d, red dashed lines). They also made 'Velcro noises' (also observed in the clinic) when pulled away from implant surfaces due to tight integration with the more textured surfaces[29,46] (Supplementary Videos 1–3). White plastic-like inner capsule formation was often also thicker with prominent banding patterns in areas of implant rippling or folding. Haematoxylin and eosin (H&E) and Masson's trichrome histology stains were carried out for each implant and time point to quantify cellular deposition and the extent of fibrous encapsulation (Fig. 2c–h and Supplementary Fig. 8). The obtained images suggest that capsule thickness was significantly reduced for SmoothSilk implants, but was significantly higher for

Fig. 2 | Breast implant surface topography affects host response and fibrosis in rabbits. a,b, Human-scale (205 cm³) breast implants explanted following 3 week (**a**) or 6 month (**b**) subcutaneous implantations in New Zealand White rabbits. **c,d,** H&E (top) and Masson's trichrome (bottom)-stained histologic sections of tissue and capsules surrounding 3 week (**c**) and 6 month (**d**) subcutaneous implants. Scale bar, 1,000 μm; original magnification, ×4. **e,f,** Fibrotic capsule thickness surrounding 3 week implants on their top subcutaneous side (**e**) or bottom (deeper tissue) side (**f**). **g,h,** Six-month top (**g**) and bottom (**h**) capsule thickness. Double capsules were observed as early as three weeks for Siltex, Microcell and Biocell implants, with strong Velcro effects upon dissection and separation of implant and tissue capsule for histology processing (Supplementary Videos 1–3). Five measurements of capsule thickness were taken for 5 different fields of view from 2 different regions of tissue, with numbers then compiled across $n = 5$ rabbits per group. **i,j,** NanoString analysis of 3 week human-scale subcutaneous implants in New Zealand White rabbits for immune markers and cytokines, compared with mock (saline-injected) controls. Patterns of downregulation (**i**) and upregulation (**j**) in the SmoothSilk group suggests differential immune modulation. In bar graphs, data are mean ± s.e.m. of biological replicates. One-way analysis of variance (ANOVA) plus Bonferroni multiple-comparisons correction; ***$P < 0.001$ and ****$P < 0.0001$ versus control; ###$P < 0.001$ and ####$P < 0.0001$ versus SmoothSilk; and ```$P < 0.001$ and ````$P < 0.001$ versus VelvetSurface. *$P = 0.0418$ (SmoothSilk versus control) and 0.0237 (Microcell versus control) (**e**); **$P = 0.002$ and ^^$P = 0.0031$ (**f**); *$P = 0.0418$, **$P = 0.0058$, #$P = 0.0314$ and ^$P = 0.0458$ (**g**); ##$P = 0.0019$ (**h**).

Siltex, Microcell and Biocell implants compared with Smooth controls (Supplementary Table 3). Capsule thicknesses for Siltex, Microcell and Biocell implants were also significantly increased when compared with those for both SmoothSilk and VelvetSurface

implants (Fig. 2e,f, Supplemental Figs. 5–8 and Supplementary Table 3). Further, in histological tissue sections of Siltex, Microcell and Biocell implants we observed wear debris within their inner capsules (Supplementary Fig. 9). Conversely, no debris was found
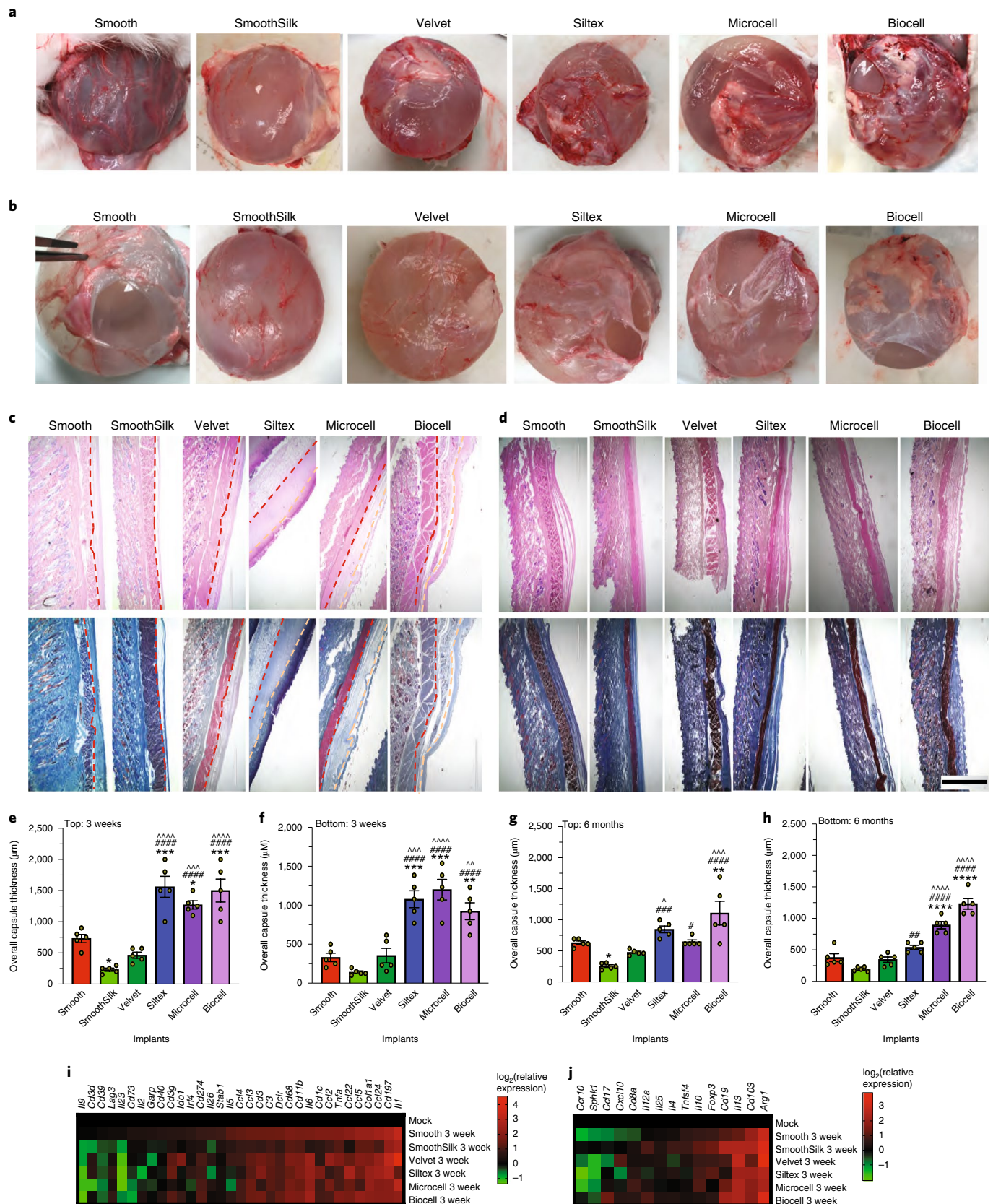
in histological tissue sections of control (traditional) Smooth, SmoothSilk and VelvetSurface capsules even 6 months after implantation. Implant capsules were also examined further with confocal microscopy staining for nuclei (DAPI), F-actin (cell cytoskeleton marker) or the macrophage marker CD68, and α-smooth muscle actin (α-SMA; a myofibroblast and surrogate fibrosis marker), confirming reduced immune and fibroblast responses with SmoothSilk and VelvetSurface implants (Supplementary Fig. 10). To further evaluate longer-term FBR and fibrosis with SmoothSilk versus traditional Smooth control and macrotextured Biocell implants, an additional follow-up study in rabbits was performed with up to one year of exposure. We observed significantly thicker fibrous capsules associated with control and Biocell implants compared with SmoothSilk implants, which exhibited improved biocompatibility up to the one year period of our study (Supplementary Fig. 11).

Furthermore, to gain additional insight into local cell and cytokine markers (that is, immune cell, inflammatory and fibroblast or fibrotic responses), we performed NanoString multiplexed gene-expression analysis to profile host-mediated tissue responses to the clinical implants in New Zealand White rabbits compared with mock (saline-injected) implant tissues (Fig. 2i,j and Supplementary Fig. 12). Our analysis shows two main clusters of genes, one with reduced RNA expression of inflammatory cytokines associated with SmoothSilk implants compared with all other implant groups tested (Fig. 2i), suggesting differential modulatory behaviour associated with each surface topography and implant group. Important markers in the first cluster include the macrophage or myeloid markers *Cd68* and *Cd11b*; inflammatory markers *Il1*, *Il6*, *Il26* and *Tnfa*; macrophage chemoattractants *Ccl3* and *Ccl4*; T cell chemoattractants *Ccl5*, *Ccl22* and *Ccl24*; and fibrosis marker *Col1a1*. The second cluster shows an increased presence of anti-inflammatory cytokine and immunoinhibitory regulatory T cell presence with SmoothSilk (highest level of expression versus other implant groups), as denoted by the T regulatory cell (T_{reg}) marker gene *Foxp3* as well as inhibitory cytokines *Il4*, *Il10*, *Il13* and *Il25* (Fig. 2j). Together, these results suggest that SmoothSilk implants are more biocompatible and produce less pro-fibrotic inflammation compared with the other implant types tested in New Zealand White rabbits.

Fibrosis prevention with miniaturized silicone implants. Following earlier confirmation of comparable surface topography between miniaturized and full-scale clinical implants, moderate volume (0.6 cm projection and 1.3 cm diameter; 0.73 cm³ volume) (Supplementary Fig. 13) miniaturized implant shells were filled with the same silicone gel for consistent softness and implant behaviour, and implanted into the subcutaneous mammary fat pad space of C57BL/6 mice for 3 and 6 weeks ($n = 5$ per implant group per time point) (Supplementary Fig. 14). Following implant retrieval, surrounding tissue capsules were stained with H&E and Masson's trichrome for histology assessment (Fig. 3a,b). Implant groups were labelled with profilometry-determined surface roughness ranges (as shown in Fig. 2e). Groups labelled 0, 4, 15, 30 and 90 μm correspond to micron-range roughness measurements, and (based on measurement of the clinical implants, as shown in Fig. 2d) are comparable to control Smooth, SmoothSilk, VelvetSurface, Siltex

and Biocell implants, respectively. Fibrotic capsular thicknesses surrounding three week and six week implants were quantified (Fig. 3c,d). Similar to the data generated in the rabbit model, capsular thickness was reduced with miniaturized SmoothSilk-like 4 μm surface roughness. The 15 μm surface roughness, similar to that of VelvetSurface implants, also significantly reduced capsule thickness. The largest 90 μm surface roughness implant group, similar to Biocell implants, resulted in an increase in capsule thickness compared with Smooth control implants at 3 weeks. This difference, however, was no longer significant at 6 weeks due to an increase in capsule thickness around the control Smooth group and a decrease in capsule thickness around the largest 90 μm roughness group (Fig. 3c versus Fig. 3d). Supporting previously reported associations between the presence of innate immune macrophages and the level of fibrotic encapsulation[37,47], quantitative fluorescence-activated cell sorting (FACS) analysis was performed on cells dissociated from capsules surrounding implants retrieved after 3 weeks (Fig. 3e) and confirmed that macrophage (CD68+CD11b+) levels correlated with observed capsular thickness. We sought to explore another immune cell population—adaptive immune T cells and how they might regulate immune-mediated fibrous capsule formation. Although T cells are reported to not be stimulated by different implant surfaces in vitro[48], they have been shown to be influenced by different implant surfaces in vivo[49]. We investigated whether different surface topographies might increase the local presence of CD4+CD25+FOXP3+ T_{reg} cells, which have previously been shown to suppress pro-fibrotic macrophages[50]. Supporting this notion, our results indicated that increasing surface roughness led to higher T_{reg} cell recruitment into tissue capsules surrounding miniaturized implants (Fig. 3f and Supplementary Fig. 15).

The balance of T_{reg} cell levels appears to be essential: it needs to be low enough to avoid extreme immune suppression, which might support immune escape of either microbial contaminants or cells going through oncogenesis, and high enough to inhibit the emergence of autoimmunity[51]. In a recent retrospective study, one group suggested that breast implants may increase the change of autoimmune incidence (by 3.46%); however, a separate study has shown inconsistent epidemiological results in this regard[52]. One limitation to such analyses is that the emergence of autoimmune diseases increases as patients age, even without the presence of breast implants[53]. One group even reported an age-adjusted increased incidence of certain rare autoimmune events in the largest prospective silicone implant cohort to date[10]. Although such phenomena were not investigated in this present study—which is focused on implant biocompatibility and fibrosis suppression—they should be considered in follow-on studies.

**Immunoprofiling responses to miniaturized silicone implants.** To investigate the acute effects of implants on the immune system, prosthetics with surface roughness of 0, 4 and 90 μm (Ra) were implanted in mammary fat pads of C57BL/6 mice for 2 weeks. Cells adjacent to the resulting tissue capsules were evaluated by pooling samples from five mice and analysed using single-cell RNA sequencing (scRNA-seq) (Fig. 4a). We used the scRNA-seq data to compare cell composition and expression signatures of the immune

Fig. 3 | Breast implant surface topography affects host responses and fibrosis in mice. a,b, H&E and Masson's trichrome-stained histologic tissue sections surrounding subcutaneous mouse-scale miniaturized implant mimics with the indicated topography that were explanted after 3 (**a**) or 6 (**b**) weeks in C57BL/6 mice. Scale bars, 1,000 μm; original magnification, ×4. **c,d**, Capsule thickness surrounding 3 week (**c**) or 6 week (**d**) implants. Five measurements of capsule thickness were taken for 5 fields of view from 2 different regions of tissue, with numbers then compiled across $n = 5$ mice per group. **e**, Quantitative FACS analysis of cells dissociated from capsules surrounding implants from each surface topography group, retrieved after 3 week implantations. **f**, FACS analysis of CD4+CD25+FOXP3+ cells as a percentage of total cell counts from dissociated explant tissue from each implant group. In bar graphs, data are mean ± s.e.m. of biological replicates in all cases. One-way ANOVA plus Bonferroni multiple-comparisons correction; ***$P < 0.001$ and ****$P < 0.0001$ versus control; ###$P < 0.001$ and ####$P < 0.0001$ versus SmoothSilk; and ```$P < 0.001$ and ````$P < 0.0001$ versus VelvetSurface.; *$P = 0.0377$ and **$P = 0.0011$ (**c**); *$P = 0.419$ and ##$P = 0.0042$ (**d**).

infiltrate that accumulated at capsule boundaries with each implant type. Counting the transcripts barcoded within each individual cell yielded a matrix of transcript expression across all individual cells (Fig. 4b), with five major clusters that were well represented by all three conditions (Supplementary Fig. 16a). Uniform manifold approximation and projection (UMAP) embedding of individual
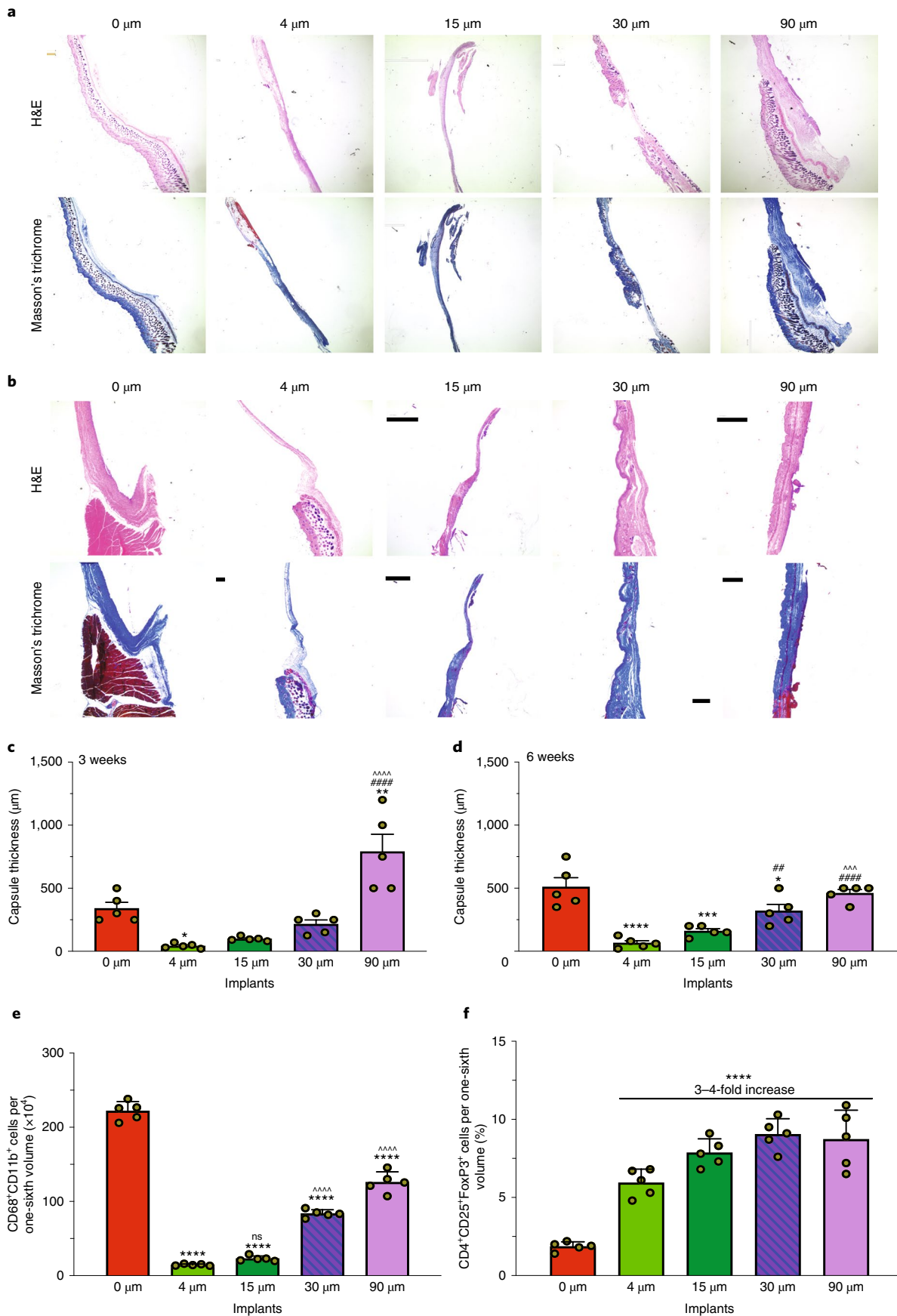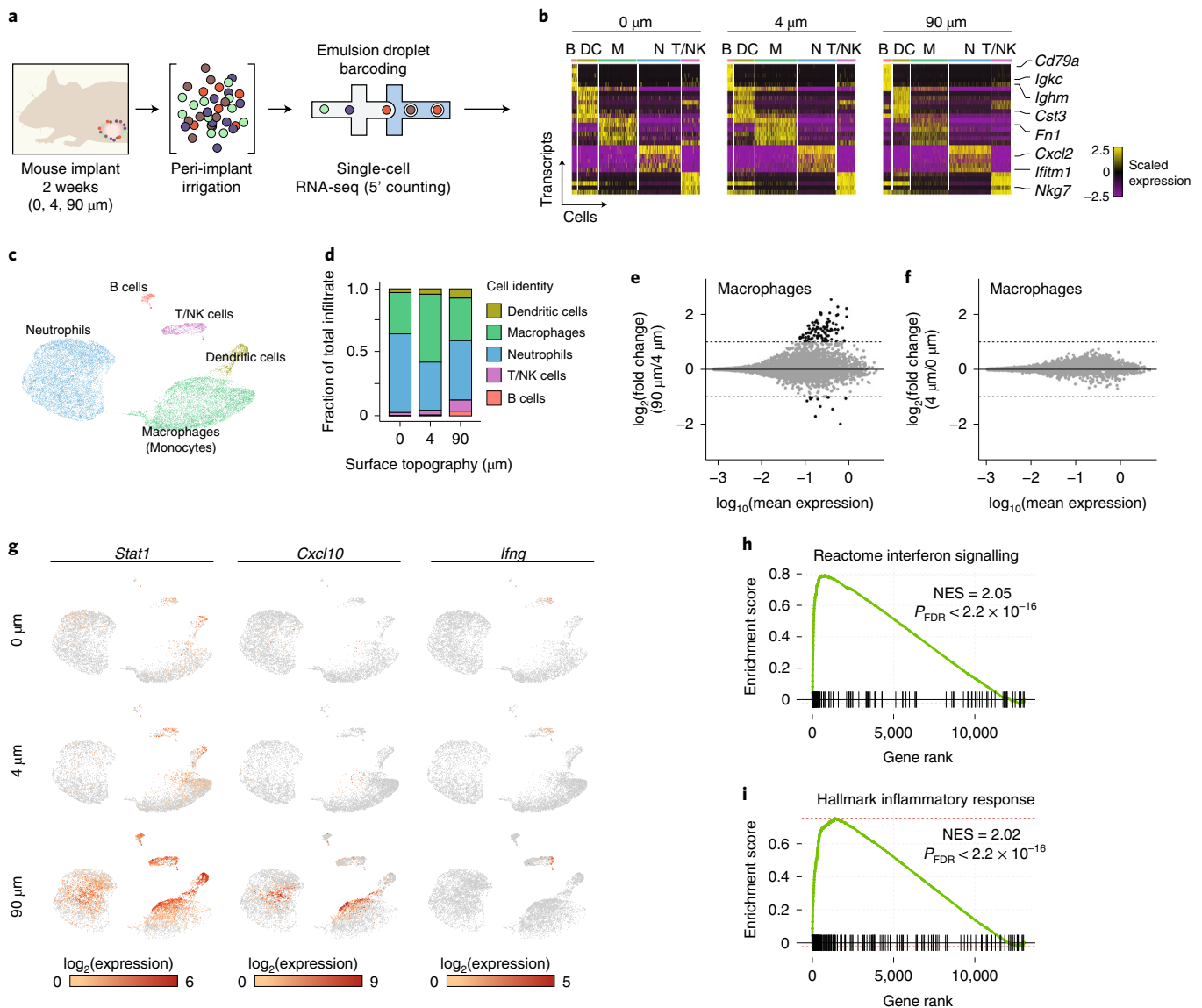
Fig. 4 | Acute immune effects two weeks after implantation revealed by scRNA-seq. a, Preparation of immune cell populations two weeks after implanting textured (90 μm) or untextured (0 and 4 μm) miniaturized breast implants. **b**, Single-cell transcriptional profiles clustered into groups by k-means clustering. B, B cells; DC, dendritic cells; M, macrophages; N, neutrophils; T/NK, T and NK cells. **c**, UMAP embedding of individual cells pooled from all three samples (0, 4 and 90 μm). Resulting clusters are classified by immune cell type on the basis of cell-specific expression profiles (Supplementary Fig. 16c). **d**, Composition of peri-capsular immune cell identities recruited to each implant site at 2 weeks, as classified in **c**. **e,f**, Gene-expression changes in macrophages found in 90 μm versus 4 μm (**e**) and 4 μm versus 0 μm (**f**) implants. Horizontal dashed lines represent the cut-off values for 2 fold-change deviation. **g**, Expression of individual inflammatory genes across cell types. **h,i**, GSEA from Reactome (**h**) and Hallmark (**i**) gene sets associated with expression changes in 90 μm versus 4 μm implants. More detailed cytokine data (by cell population) are shown in Supplementary Fig. 18. All subpanels reflect representative data from in vivo experiments performed once; scRNA-seq was run on one sample pool per treatment group (from $n = 5$ biological replicates). NES, normalized enrichment score.

cells from all three samples confirmed five distinct clusters (Fig. 4c), which readily corresponded to individual cell types using standard cell-type-specific markers (Supplementary Fig. 16b). Based on the expression of these markers, clusters were defined as neutrophils, B cells, dendritic cells, macrophages (including monocytes) and T or natural killer (NK) cells (Fig. 4c).

Implant topology had a clear effect on the acute composition of the immune infiltrate recruited to the implant site at this two week time point (Fig. 4d). Most notably, the highly textured 90 μm implant significantly increased the proportion of both T cells and B cells compared to the 4 μm implant. Between these two conditions, the proportion of T cells increased 2.4-fold (Fisher exact test,

false-discovery rate-adjusted P-value ($P_{FDR} = 3.67 \times 10^{-16}$) and the proportion of B cells increased 5.5-fold ($P_{FDR} = 3.67 \times 10^{-16}$) in the 90 μm sample. By contrast, the differences between the 4 μm and 0 μm implants were smaller in magnitude. The highest magnitude changes between 4 μm and 0 μm implants were a 1.6-fold increase (adjusted P-value ($P_{adj} = 3.67 \times 10^{-16}$) in the proportion of macrophages, consistent with a smaller induced immune response. In addition, to examine the potential for shifts in fibroblast cell response, we used flow cytometry of retrieved capsule tissues that were dissociated into single-cell suspensions, and measured the myofibroblast markers α-SMA and fibroblast activation protein (FAP) (Supplementary Fig. 17a,b). We observed a minor increase
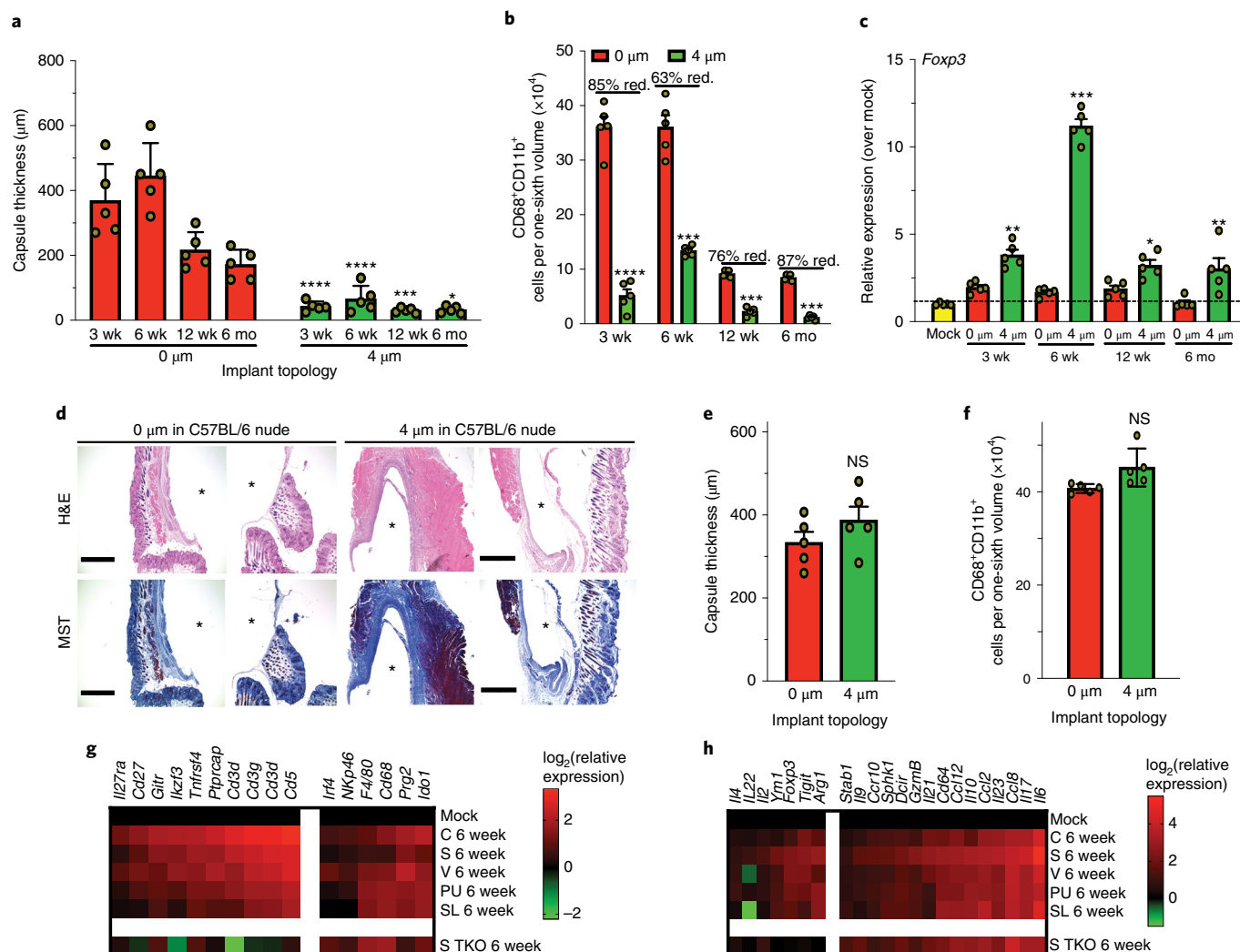
Fig. 5 | Long-term kinetics of host immune response to 0 and 4 µm implants in wild-type mice, and testing in nude mice implicating a T-cell-regulated mechanism. a, Quantification of fibrotic capsule thickness surrounding miniaturized implant mimics with the indicated topography subcutaneously implanted for 3, 6 and 12 weeks (wk) and 6 months (mo) in wild-type C57BL/6 mice. Five measurements of capsule thickness were taken from 5 fields of view from 2 different regions of tissue and compiled across $n = 5$ mice per group. **b**, Quantitative FACS analysis of cells dissociated from capsules surrounding implants from each group. Per cent reduction (red.) compared with Smooth control is shown. **c**, Quantitative PCR (qPCR) analysis of *Foxp3* expression levels in explanted tissue from each implant group relative to a mock implant control. **d**, H&E and Masson's trichrome-stained (MST) histologic tissue sections surrounding subcutaneous miniaturized implants that were explanted after three weeks in C57BL/6 nude mice. Scale bar, 1,000 µm; original magnification, ×4. Asterisks denote original location of implant. **e**, Fibrotic capsule thickness surrounding 3 week implantations in C57BL/6 nude mice. **f**, Quantitative FACS analysis of cells dissociated from capsules surrounding implants from each surface topography group, retrieved after 3 week subcutaneous implantations in C57BL/6 nude mice. **g,h**, Two gene subsets (decreased versus increased in the 4 µm group) determined by NanoString analysis of subcutaneous tissue associated with 6 week implants in C57BL/6 and C57BL/6 nude (TKO) mice, relative to mock (saline-injected) controls. MGI gene symbols are shown in parentheses: *F4/80* (*Adgre1*), *NKp46* (*Ncr1*), *Gitr* (*Tnfrsf18*), *Il17* (*Il17a*), *Il23* (*Il23a*), *Cd64* (*Fcgr1*), *Dcir* (*Clec4a2*) and *Ym1* (*Chil3*). All bar or line graph data are mean ± s.e.m. of biological replicates. One-way ANOVA plus Bonferroni multiple-comparisons correction; ***$P < 0.001$ and ****$P < 0.0001$ for comparisons with control; *$P = 0.0228$ (**a**); **$P = 0.0028$ (3 week), *$P = 0.02$ (12 week) and **$P = 0.0015$ (6 mo) for comparisons with control (**c**). NS, not significant; C, control (smooth); S, SilkSurface mould; V, VelvetSurface mould; PU, polyurethane foam imprint; SL, salt-loss manufacturing.

in α-SMA⁺FAP⁺ activated fibroblasts between 0 and 90 µm sample groups at 2 weeks after implantation. However, biomaterial-induced fibroblast activation markers are probably more heterogeneous than our designed study could capture by examining FAP alone, and future studies could focus on identifying a broader set of fibroblast cell phenotypes.

Differences in expression between 90 µm and 4 µm conditions revealed a significant upregulation in the expression of individual genes involved in inflammatory immune signatures, including pro-inflammatory transcription factors and cytokines or chemokines and their receptors (Fig. 4e). Specifically, expression of STAT1, a pro-inflammatory transcription factor that regulates immune activation downstream of interferon, was increased across all immune cell populations[54,55]. We also observed strong upregulation of pro-inflammatory chemokines, including CXCL10, which is expressed by leukocytes, neutrophils, eosinophils and monocytes to recruit T cells, B cells, NK cells and macrophages to sites of inflammation[56]. In particular, 90 µm implants induced upregulation of the broadest class of inflammatory cytokines or chemokines across immune cell types, consistent with activation of innate and

adaptive immune responses (Supplementary Fig. 18). Additionally, we observed increased expression of interferon-γ in a portion of T and NK cells. Interferon-γ is a potent inflammatory cytokine that shapes immune responses by activating macrophages, inducing B cell switching and altering T helper response[57]. Consistent with increased pro-inflammatory effects, the CD3+CD8+ cytotoxic effector T cell subset increased more significantly in the 90 μm group at both 2 and 4 weeks after implantation compared with both the 0 and 4 μm implant groups (Supplementary Fig. 17c,d). In addition, while there were similar levels of CD3+CD4+CD25+FOXP3+ T$_{reg}$ cells across the 4 and 90 μm groups, a net increase in the ratio of cytotoxic T cells to T$_{reg}$ cells was apparent only in the 90 μm group ($P < 0.001$) (Supplementary Fig. 17c–e).

To confirm altered engagement of broader cell signalling networks, we pooled transcripts across individual cell types and examined fold changes of individual genes induced by each surface topography. We observed profound upregulation of a large number of genes across all cell types in the 90 μm samples (macrophages shown in Fig. 4f), that was not observed in the 4 μm or 0 μm samples (Fig. 4g). To assess whether these increased transcripts corresponded to activation of gene sets, we used gene set enrichment analysis (GSEA) using Hallmark and Reactome gene sets and found strong upregulation of gene sets involved in inflammation and interferon response (Fig. 4h,i, $P < 2.2 \times 10^{-16}$). These gene sets were not significantly increased in the 4 μm compared with the 0 μm implants ($P > 0.05$). Interestingly, the 90 μm but not 4 μm or 0 μm implant topography induced a mixed macrophage phenotype, with high expression of inflammatory M1-like signatures but also high expression of the arginase 1 gene (*Arg1*), a marker of anti-inflammatory M2-like macrophage signatures (Supplementary Fig. 16c). This finding indicates that these implants induce a complex landscape of immune signalling that is largely pro-inflammatory, as well as anti-inflammatory innate immune signalling that constrains overall inflammatory response. Our findings indicate that the highly textured 90 μm implant topology induces acute immune effects as early as two weeks, which results in both notable B and T cell infiltration, as well as strong activation of the innate immune response. Overall, immune activation is clearly visible after two weeks with the 90 μm implants, but was not observed with 4 μm or 0 μm implants.

Optimized surface topography results in long-term fibrosis attenuation in vivo. Based on positive short-term results in C57BL/6 mice, miniaturized SmoothSilk (4 μm) implants were used for a long-term efficacy study of up to 6 months. Miniaturized Smooth control (0 μm) and SmoothSilk (4 μm) implants were retrieved after 3, 6, 12 and 24 weeks for capsule assessment (Supplementary Figs. 19 and 20). Masson's trichrome and H&E histological staining confirmed significant reduction in fibrosis with the miniaturized SmoothSilk (4 μm) implants compared

with miniaturized Smooth control implants (Fig. 5a). Flow analysis for responding CD68+CD11b+ macrophages isolated from tissue surrounding implants at each time point indicated significantly reduced cell numbers for mini SmoothSilk implants (Fig. 5b and Supplementary Fig. 21). This finding was confirmed by immunofluorescence images obtained from histology sections showing reduced macrophage CD68 staining surrounding mini SmoothSilk as well as mini VelvetSurface implants (Supplementary Fig. 22). In addition, as suggested above, we observed decreasing immunologic responses over time for control material implants at longer-term (12 week and 24 week) time points (Fig. 5b), as fibrotic encapsulation becomes more complete[47].

Anti-fibrotic efficacy of optimized surface topography is T-cell-dependent. Supporting a potential immune-based mechanism for SmoothSilk-mediated alteration of observed fibrotic response, tissues surrounding miniaturized SmoothSilk-mimic (4 μm) implants showed significantly higher expression levels of the regulatory T cell marker FOXP3 up to 6 months after implantation in wild-type C57BL/6 mice (Fig. 5c). To determine whether there was causality and a dependent relationship between the anti-fibrotic effects of 4 μm roughness and T cells, both 0 μm and 4 μm implants were placed subcutaneously in the mammary fat pad of T-cell-deficient C57BL/6 nude mice for 3 and 6 weeks. Unlike the observations in wild-type mice, fibrotic capsule thickness was thicker for 4 μm implants and similar in scale that seen for 0 μm controls (Fig. 5d,e and Supplementary Fig. 23). Quantitative FACS analysis of cells dissociated from tissue capsules isolated from T-cell-deficient C57BL/6 nude mice after 3 week implantations also showed that macrophage (CD68+CD11b+) presence was increased around 4 μm implants and no longer significantly reduced compared with levels around 0 μm controls (Fig. 5f versus Fig. 5b). Confocal staining for macrophage presence in tissue capsules surrounding 4 μm implants retrieved after 6 weeks also verified an increase in local macrophage presence with concomitant T cell removal (Supplementary Fig. 22, bottom right). Collectively, these results indicate that T cells are both necessary and required for reductions in macrophage response as well as capsular thickness.

To gain additional insight into how implant topography affects local tissue microenvironment cell and cytokine responses, including immune (macrophage and T cell) and fibroblastic or fibrotic presence and behavioural phenotype[58], we performed a comprehensive multiplexed NanoString expression array experiment on retrieved fibrotic capsule tissues from both wild-type and T-cell-deficient C57BL/6 nude mice (Fig. 5g,h and Supplementary Fig. 24). Similar to the observations in the rabbits, two gene-expression groups were identified: (1) one associated with SmoothSilk-like (4 μm) and inflammatory suppression (decreased RNA expression compared with controls and other implant groups), and (2) on where 4 μm

Fig. 6 | Human breast tissue explant histology and immune profiling. Breast capsule tissue samples were analysed from 21 human recipients (Supplementary Table 5) of either SmoothSilk (1–5), Smooth (6–10) or Biocell (healthy: 11–15; ALCL: 16–21) implants. **a**, H&E and Masson's trichrome staining of histologic sections of tissue and capsules surrounding implants. Scale bars, 1,000 μm; original magnification, ×4. **b**, Fibrotic capsule thickness surrounding implants. Data are mean ± s.e.m. of biological replicates. One-way ANOVA; ***$P < 0.001$ (Smooth versus SmoothSilk); ****$P < 0.0001$ (SmoothSilk versus Biocell). **c**, High-magnification images of capsule tissue for different implant groups (as specified) showing immune cell infiltration. Scale bars, 100 μm. ALCL, anaplastic large cell lymphoma. **d,e**, NanoString analysis for capsule microenvironment cell and cytokine response markers, plotted in heat maps showing absolute transcript counts normalized to housekeeping genes (*ACTB*, *HPRT1*, *CLTC* and *TUBB5*) to account for sample processing variabilities. **d**, Analysis of explants from healthy recipients of SmoothSilk, Smooth controls or Biocell implants. **e**, Analysis of explants from patients with ALCL of paired capsule specimens of disease capsule (D) and from the contralateral non-diseased (ND) breast of a recipient of Biocell implants, three additional unpaired Biocell-associated ALCL capsules, and two from patients with breast implant-associated illness (BII), both of whom had ruptured implants. Pink indicates values are above upper scale limit. $n = 5$–6 individuals per implant group. HGNC gene symbols are shown in parentheses: *TGFB* (*TGFB1*), *CD73* (*NT5E*), *aSMact* (*ACTA2*), *IL10R1* (*IL10RA*), *CD11B* (*ITGAM*), *CD39* (*ENTPD1*), *GARP* (*LRRC32*), *DCIR* (*CLEC4A*), *CD45RO* (*PTPRC*), *mMGLs* (*CLEC10A*), *CD66B* (*CEACAM8*), *CD64* (*FCGR1A*), *CD197* (*CCR7*), *F4/80* (*ADGRE1*), *GITR* (*TNFRSF18*), *CD11A* (*ITGAL*), *CD103* (*ITGAE*), *CD127* (*IL7R*), *CD3* (*CD3E*), *IL1* (*IL1A*), *IL17* (*IL17A*), *IL23* (*IL23A*), *LIGHT* (*TNFSF14*), *NKP46* (*NCR1*), *CD25* (*IL2RA*) and *TNFA* (*TNF*). Statistical analysis for NanoString is described in Methods.

implants induced increases of anti-inflammatory cytokine and immunoinhibitory regulatory T-cell-response transcripts (the highest level of RNA expression versus all other implant groups). Notable

markers in these two groups that share similar trends also observed in the rabbits include: in set (1), macrophage markers *Cd68* and *F4/80*, T-cell-stimulation markers *Cd27* and *Tnfrsf4* (which encodes
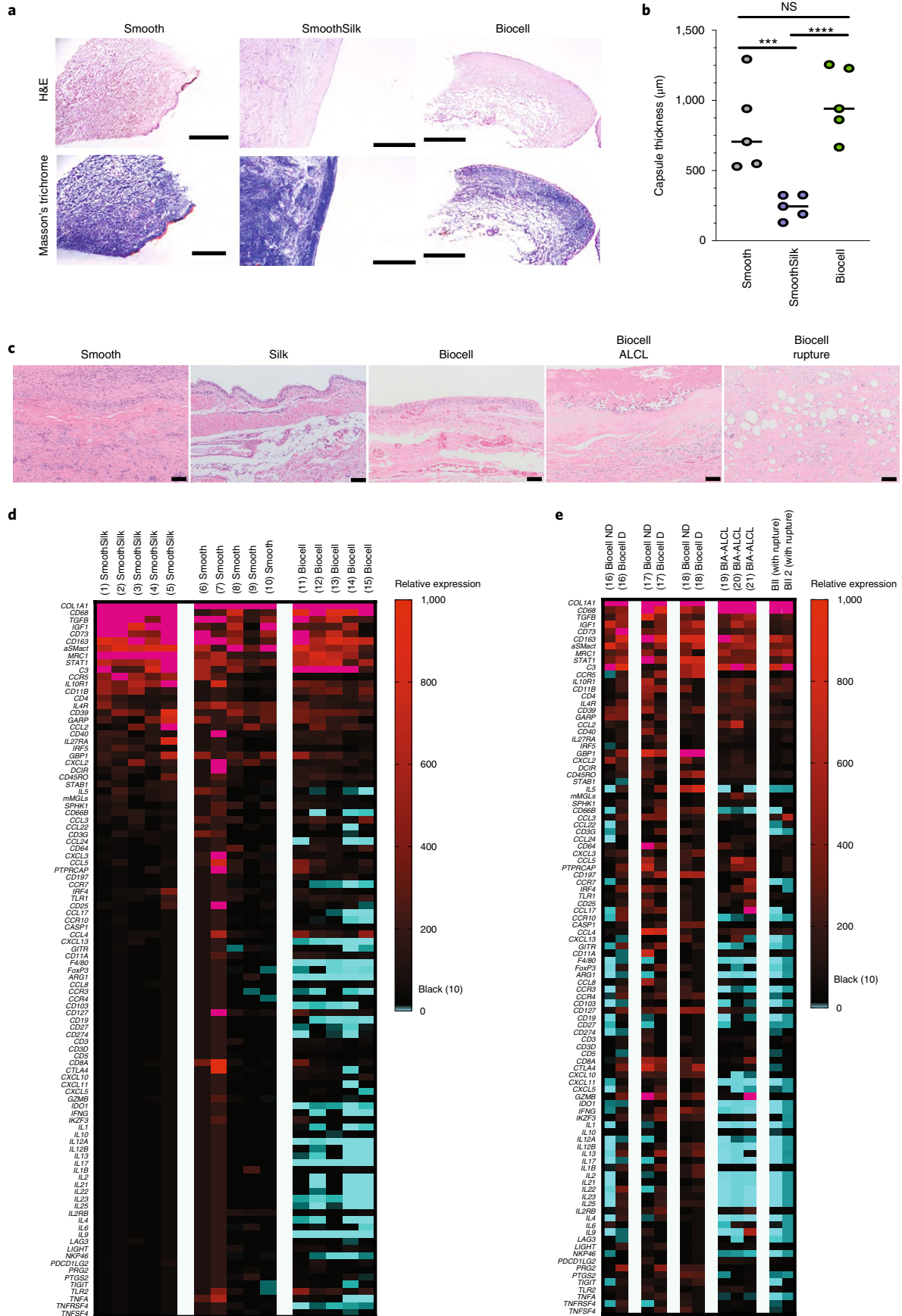
the OX40 receptor) and the macrophage and T-cell-stimulatory receptor gene *Il27ra*; and in set (2) genes encoding inhibitory cytokines *Il4* and *Il10*, the leukocyte chemoattractant *Ccl8* and the T$_{reg}$ marker *Foxp3*. In each gene set, there was a subset of factors (left side of each heat map) where RNA expression that was increased in wild-type mice was instead reduced to or below background levels in the T-cell-deficient mouse model, potentially implicating their lost upregulation with the observed finding that 4 μm implants lost the ability to inhibit thicker fibrous encapsulation in T-cell-deficient mice (Fig. 5d,e). Although numerous factors showed common patterns of response between implantation of different breast implant topographies in both mice and rabbits, there were also a few factors that showed less consistency. It is possible that this is due to species-specific differences between mouse and rabbit models.

Validation of findings with human patient samples. To further corroborate the preclinical findings in our fibrotic C57BL/6 mouse and New Zealand White rabbit animal models, we sought to compare them to clinical human breast implant-associated capsular tissue. Specimens were collected in a uniform fashion from the same anatomical capsule layer during revision surgeries from 21 female recipients who had received different breast implant types: traditional Smooth (from five healthy individuals), SmoothSilk (five healthy individuals), or Biocell (five healthy individuals, three with one breast diagnosed with ALCL and three additional unpaired ALCL samples). We tracked the disease state, type of implant and duration of implant for each patient included in our study (Supplementary Table 4). Histologic analysis (H&E and Masson's trichrome staining) of the thickness of capsular tissue correlates with our observations in mice and rabbits, with SmoothSilk implants having a thinner capsule than Smooth and Biocell implants (Fig. 6a,b). Additionally, higher-magnification H&E images of capsules from different implant groups were acquired to better determine the presence of immune cell infiltrates in capsular tissue (Fig. 6c).

To better unravel the inflammation states in human tissue explants, we used multiplexed NanoString RNA analysis to probe for markers of immune cells and inflammation states in breast implant capsules. We collected tissue explants from 21 human recipients: 15 healthy individuals and 6 patients with BIA-ALCL. From three of the six patients with BIA-ALCL who had received Biocell implants in both breasts, we collected paired capsule specimens of either diseased or contralateral normal, non-diseased breast within the same patient (Fig. 6d,e). The recipients had previously received implants for periods of time ranging from 1–11 years (Supplementary Table 4), enabling us to evaluate chronic levels of inflammation. The RNA analysis showed that while capsules from traditional Smooth implants displayed some minor differences from SmoothSilk, there was diminished expression of many genes in capsules taken from Biocell implants (Fig. 6d). This pattern of diminished expression in capsules surrounding Biocell implants was also preserved in a number of healthy, non-diseased contralateral breasts in two patients with early, non-invasive stage BIA-ALCL, as well as additional unpaired BIA-ALCL patient (diseased) capsule samples (Fig. 6e). Our observations from this human pilot study suggest that implant texture indeed differentially alters host response as a function of implant surface topography.

In summary, we have studied the foreign body immune responses to silicone implants with a range of surface topographies, and shown that surface roughness is an influential parameter in controlling host immune reactions and fibrotic encapsulation. Our findings suggest that implants with roughness of 4 μm provoked the least amount of inflammation and FBR among the surfaces studied across mouse and rabbit models and samples from human recipients. This implant surface displayed the highest positive skewness and contact points per surface area among the tested implant surfaces. FACS and gene-expression analyses in wild-type and T-cell-deficient C57BL/6 mice suggest a potential role for

T cells in surface-mediated immune responses. Host responses associated with the implant topographies described here may have implications for improved design of other implanted biomedical devices. Furthermore, our results could potentially help inform regulatory agencies and physicians in their efforts to better mitigate immune-related complications with breast implants.

Methods

Materials. Reagents for in vitro experiments were purchased from Life Technologies, unless otherwise mentioned. The antibodies (fluor-conjugated anti-mouse LY6G/LY6C (also known as GR1), CD11b, CD4, CD25, FOXP3 and CD68) were purchased from BioLegend and used as described below. The CD11b (anti-mouse/human) antibody (BioLegend) was used to detect CD11b in both mouse and rabbit. Cy3-conjugated anti-mouse α-SMA antibody was purchased from Sigma-Aldrich.

Human-sized, commercially available silicone breast implants. The human-sized, full-scale silicone breast implants used for this study represent the most commonly used surfaces among breast implants approved by US and/or EU regulatory agencies. All commercially available breast implants were chosen from 'off-the-shelf' units in their original sterile packaging, with volumes between 100 and 220 cm³ to be used in the New Zealand White rabbits. The surgical procedure to insert the implants followed the current state of the art for primary breast augmentation surgery, including the use of no-touch techniques, such as with a sterile insertion funnel device. The surgical technique was designed and initially supervised by one of the senior authors, board-certified plastic surgeon (M.S.), to fully reproduce the sterility used in the human procedures. All the procedures were performed by authorized and trained veterinarians and researchers at MIT. The insertion of the human-sized implants followed strictly the directions for use specifications from the manufacturers.

Miniaturized implant manufacture. Miniature implants with surfaces in five different texture ranges were made with round moulds with a 1.3 cm base and 5.93 cm projection (tiny moulds). Each surface type requires a base shell created by silicone dispersion with a specific viscosity documented in Establishment Labs' controlled manufacturing process documents. All the base shells included a barrier layer that prevents silicone gel bleed, as is the case in all breast implants marketed for human use. Miniaturized implants with a smooth surface were produced with base shells with no additional texturization. Miniature SmoothSilk implants were produced using moulds with the architecture of the SmoothSilk surface. The base shells were detached from the moulds and inverted to expose the SmoothSilk surface on the outside of the Shell. The same procedure was followed with moulds with the inverse of the VelvetSurface to produce VelvetSurface shells. Salt-loss textured shells were made by dipping the base shells into a high-viscosity silicone dispersion that was heated without curing and then covered with salt grains. After heating the silicone, the moulds were dipped into a lower-viscosity silicone dispersion to deposit a thin layer over the salt grains. After curing, the moulds with the textured shells were placed in warm water to dissolve the salt grains through the thin layer of silicone. Finally, the shells were brushed to open the pores left by the salt grains. Polyurethane foam imprint shells were made by dipping moulds with the base shells into a high-viscosity silicone dispersion that was baked without curing and then covered with a polyurethane foam. The complex of tiny mould, base shell and polyurethane foam was placed in the oven. The polyurethane foam was removed from the shells before the curing cycle ended, and the shells were re-introduced into the oven to complete the curing process. Regardless of the surface type, all the miniature implants were patched, filled, packaged and dry-heat-sterilized as described in Establishment Labs' manufacturing process controlled documents.

Scanning electron microscopy. Implant morphology and topography were studied by SEM. Samples were prepared for imaging by first placing shells from each implant group (human and mouse scale) on conductive carbon paper and then coating with ~10 nm of gold/palladium using a Hummer 6.2 Sputter Coater System. Coated samples were imaged using the JEOL-JSM-5600LV Scanning Electron Microscope with 2.0–15.0 KV acceleration voltage. For determining the most representative images, three SEM images were acquired for each of five different samples per implant group (mouse and human scale) before image selection.

Non-contact profilometry and surface friction. Samples, approximately 5 cm² in area, from the base, radius and anterior surface of each shell were cut from three representative devices for each surface implant group. Shell pieces were cleaned with 99% isopropyl alcohol and wiped until there was no gel or particle debris on the shell. On an anti-vibration table, samples were placed under the ×20 lens of a non-contact profilometer (μSurf Mobile). Samples were adjusted until there was a 90° angle between the surface of interest and the lens, and images were focused using the μSoft Metrology program. Smooth surfaces were acquired in automatic mode, but if the topography was unknown, upper and lower z-axis limits were

manually adjusted. Using the confocal program visualization mode, the upper and lower z limits were set on the observed image with both focusing extremes appearing completely black. Next, program visualization was set to microscope mode and brightness to automatic (with the caveat that no areas appeared red due to overexposure). x- and y-axis limits were set so that the total measured area was $4\,mm^2$ (that is, with a ×20 lens, the 3 × 3 option corresponding to a stitching area of $4.69\,mm^2$ was selected). Five images and measurements were then captured per sample for each of their anterior, base and radial sections. Data were subsequently analysed with μSoft Analysis software following ISO 25178: Geometric Product Specifications (GPS)—Surface texture: 3D areal. Average measurements and standard deviation of the characteristics were recorded. ISO 14607: 2018 Non-active surgical implants—Mammary implants—Particular requirements also served as a reference document.

For determination of comparative static and dynamic average friction coefficients of different breast implants, testing was performed by Akron Rubber Development Laboratory. Specimens were soaked in Ringer solution for 2 min and then prepared by mounting a 2.5-inch (6.35 cm) section of each implant surface shell on a steel plate. Each specimen was then pulled at 6 inch min^{-1} across a glass substrate covered with 45 ml Ringer solution and each sample was loaded with a 200 g weight. Testing was then carried out following the ASTM D 1894-14 Standard Test Method for static and kinetic coefficients of friction of plastic film and sheeting.

X-ray photoelectron spectroscopy analysis. XPS analysis was performed with a Physical Electronics Model PHI 5000 Versaprobe II instrument with a monochromatic Al K-alpha X-ray source (1,486.6 eV), operating at a base pressure of 3.7×10^{-9} Torr. For analysis purposes, five samples from each implant group (mouse and human) were analysed with five measurements from random shell surface areas in each of three acquired runs per sample.

Experimental animals and implantation surgeries. Animal studies were performed at multiple institutions. All animal surgeries and protocols were carried out in complete compliance with all relevant ethical regulations, as approved by the MIT Committee on Animal Care, (IACUC). In addition, all surgical procedures as well as the post-operative care were supervised by the veterinary staff of MIT Division of Comparative Medicine. Implant procedures were similar to those previously described[37,39], with some exceptions. Specifically, immune-competent 8-week-old, female C57BL/6 mice (Jackson Laboratory) were anaesthetized with 3% isoflurane, and then their bellies (along the teats) or hind flanks (with either location containing mammary fat pads) were shaved and sterilized using betadine and isopropanol. We ultimately permanently adopted the hind flank position to allow for more loose skin as well as keep the implants away from mouse interference (both of which contributed to eliminating issues with incision line dehiscence). Ophthalmic ointment was used to prevent dry eyes, and all mice received 1 mg kg^{-1} slow-release buprenorphine subcutaneously as a pre-surgical analgesic, plus 0.3 ml 0.9% NaCl (to prevent dehydration). Blunt dissection was used to open implant pockets for insertion of one ~8-mm-wide and 5-mm-high 'demi'-scale (comparing the width of a human to that of a mouse) breast implant (taken from pre-packaged sterile containers, described above) away from the minimal incision line for each mouse. The skin was then closed with wound clips and tissue glue.

For procedures in female 3–4 kg New Zealand White rabbits (Charles River), slow-release buprenorphine (0.12 mg kg^{-1}) was preoperatively administered as an analgesic. Rabbits were then sedated by intramuscular ketamine (35 mg kg^{-1}) and xylazine (3 mg kg^{-1}). Portions of their lower belly, left and right chest and hind shoulders were shaved; the latter, containing mammary fat, was also sterilized using surgical scrub. This hind upper shoulder area was also chosen due to thick, flexible skin (similar to that of a human) and to prevent rabbits from scratching or biting at and complicating implant response. The former sites were shaved to allow for placement of electrocardiogram equipment for heart rate monitoring. Ophthalmic ointment was used to prevent dry eyes, an assisting nose cone or laryngeal airway mask was kept in place for supplemental flow-by 2% isoflurane, with a handheld respiration monitor and thermal probe to follow additional vital signs. Animals were kept on circulating warm water blankets and covered during the entire procedure to maintain body temperature.

Surgeons wore sterile gloves and gowns, and a sterile drape was placed before a minimal 2.5 or 3 to 4 cm incision was made. Blunt dissection was then used to open one implant pocket for insertion of one breast implant with its margin at least 1–2 cm away from the minimal incision line. Implants were tilted out from vendor-supplied, pre-packaged sterile containers into sterile insertion sleeves (pre-wet slightly with sterile saline at 37 °C), which were used to place all larger-diameter implants through minimal incisions (with greater texturing requiring slightly (~1 cm) larger incision lines, at the upper range indicated above; despite this, to prevent deconvoluting mixed immune responses (FBR to the implant and wound healing response to the incision wound field) in the same volume of tissue, in each case, implants were placed in a more lateral position (away from the incision just to the side of the spinal column) following blunt dissection. Skin incisions were then closed in predominantly two layers: an intradermal layer with absorbable 4-0 suture, and then a horizontal mattress

suture for added strength. The incision line was covered with adhesive, bolstered at its four corners with some tissue glue. In rare cases where rabbits were found to aggressively scratch at their implants, risking dehiscence of their closed incision line (less than 5% of the time), the need for additional use of an ace bandage-like body wrap was used at the discretion of a veterinarian. We also clipped the nails of the rabbits on the day of implantation to avoid such issues during the initial weeks of healing. In all cases, rabbits were monitored for recovery, and meloxicam (0.3 mg drug/kg body weight, injected subcutaneously) was administered once a day for the first three days following surgery.

Human tissue source. De-identified clinical specimens of capsules collected from recipients of Smooth (Allergan) or Biocell (Allergan) implants were collected following institutional review board approval at MD Anderson Cancer Center and acquisition of informed consent. Similarly, capsule tissue from recipients of SmoothSilk breast implants (Motiva) were obtained from the Establishment Labs tissue bank, which collected specimens following Scientific Ethical Committee of the Costa Rican Institute for Research and Teaching in Nutrition and Health Foundation. Details of patient information are included in Supplementary Table 4. Following collection, all human (female) samples were de-identified before shipment for processing, assays and analysis, following which we de-blinded the samples to label and finalize arrangement for presentation.

Retrieval of tissues and implant materials. Procedures were carried out similar to those previously described[37,39] and at time points as specified in the figures. In brief, animals were euthanized and an incision was made for collection of implants and their surrounding tissues for various analyses, including histology, FACS and expression studies. For all samples, incisions were made in the skin with a wide margin around the implants for careful isolation of materials and to avoid disrupting the implant–tissue interface for post-retrieval analyses.

Imaging of the retrieved capsules. Multiple photographs and videos were taken of retrieval procedures and of retrieved implants and their surrounding tissue at each retrieval time point. This was done to monitor incision lines, the lack or presence of strong inflammation or encapsulation events, as well as short-term and long-term tissue–implant interactions.

Cell sorting. The samples were prepared for scRNA-seq by gently agitating the retrieved tissue, implant, and fluid for 5 min. The suspension was passed through a 70 μm filter to remove debris. At this point all samples from the same group were pooled into one 50 ml conical tube. The samples were centrifuged at 300g at 4 °C for 5 min. The supernatant was aspirated and 5 ml of red blood cell lysis buffer was added. After 5 min at 4 °C, RPMI1640 + 10% fetal bovine serum (FBS) was added to stop the reaction. The cells were centrifuged again at 300g at 4 °C for 5 min. The supernatant was aspirated, and the cell pellet was resuspended in 1 ml of RPMI1640 + 10% FBS and a cell count was obtained using a Countess 2 FL Automate Cell Counter. Propidium iodide Ready Flow Reagent (ThermoFisher) was added to the cells according to the manufacturer's instructions to stain dead cells. One million live cells were sorted into a 15 ml conical tube containing 1 ml RPMI1640 + 10% FBS using a Sony MA900 cell sorter. Single-cell suspensions were taken to Baylor College of Medicine for next-generation sequencing.

scRNA-seq analysis. Non-adherent cells adjacent to implanted capsules were obtained by irrigating peri-capsular space with sterile saline and processed on the 10x Chromium platform for 5′ scRNA-seq according to the manufacturer's instructions. The resulting libraries were sequenced on an Illumina NovaSeq 6000 flow cell. Transcripts in each cell were counted using the 10x Cell Ranger 5.0.1 pipeline, with genome mapping to the mm10 genome build using STAR v2.7.2a. To identify immune cell populations, the scRNA-seq data was visualized using UMAP embedding in Loupe Browser 5.0. At this stage, five cell populations were readily apparent. The resulting clusters were assessed for the expression of common immune cell marker genes and were then classified as specific immune cell types on the basis of their expression profiles. The cell identities of each of the five clusters were resolved using the following markers: CD3E and PRF1 (T cells and NK cells), CD19 (B cells), CSF1r and FN1 (monocytes and macrophages), FLT3 (dendritic cells), and LY6G and HDC (neutrophils). On the basis of these markers, individual cell barcodes were assigned to their corresponding immune cell type in the Loupe Browser.

To assess changes in the infiltrate immune composition, changes of cell proportions were calculated between each implant's surface topology for each immune cell type. The significance of these changes was calculated using Fisher's exact test in R (v3.6.1), and the resulting P-values were adjusted using the Benjamini–Hochberg false-discovery rate correction method. GSEA was performed using the fgsea R package.

Immunofluorescence and confocal microscopy. Immunofluorescence imaging was carried out as previously described[37–39], and used to determine immune population and fibrotic responses. Implants were retrieved from mice and rabbits as described above and fixed at 4 °C with 4% paraformaldehyde. Later, samples were washed twice with KREBS, permeabilized for 30 min using 0.1% Triton X-100,

and then blocked for 60 min with 1% bovine serum albumin. Next, the samples were stained for 60 min with a cocktail consisting of DAPI (500 nM), marker probes (1:200 dilution in 1% bovine serum albumin solution) as noted in displayed figures (mouse antibodies listed under FACS analysis). Following staining, samples were washed 3 times with 0.1% Tween-20 and kept in glycerol (50%). Samples were imaged in glass-bottom plates using a confocal microscope (LSM700, Carl Zeiss Microscopy). For rabbit cell staining, DAPI, anti-human CD68 Alexa Fluor 647-conjugated antibody (Clone KP1, catalogue (cat.) no. sc-20060, Santa Cruz), and Cy3-conjugated anti-mouse α-SMA antibody (Sigma-Aldrich) were used in conjunction with the above BioLegend (anti-mouse/human) CD11b–Alexa Fluor 488 antibody.

Histological processing and quantification. Retrieved samples were fixed overnight with 4% paraformaldehyde at 4 °C, as indicated above. Tissue-embedded samples were then moved to 70% ethanol. Samples were then processed for paraffin embedding, sectioning and staining according to standard histological methods (Masson's trichrome or H&E staining).

For quantification of implant capsules, consecutive tissue sections stained with H&E and Masson's trichrome were compared in parallel and capsule thickness was measured at 5 places along the implant–tissue boundary for each implant ($n = 5$ per group per time point), for a total of 5 sections for both the upper as well as lower poles or sides of the implants.

qPCR analysis. As previously described[37,47], RNA was isolated from samples snap-frozen in liquid nitrogen immediately following excision, using the TRIzol protocol (Invitrogen). Given thorough sample homogenization, displayed gene-expression signatures are representative of host response on and/or around retrieved implants. All samples were normalized by loading 1 μg total RNA in all cases for reverse transcription using the High Capacity cDNA Reverse Transcription kit (cat. no. 4368814; Applied Biosystems). cDNA (1:20 dilution) was amplified by qPCR with the primers 5′-GCCTTCAGACGAGACTTGGAA-3′ and 5′-CTGGCCTAGGGTTGGGCATT-3′ for *Foxp3* and normalized to mouse *Actb* (primers 5′-GCTTCTTTGCAGCTCCTTCGTT-3′ and 5′-CGGAGCCGTTGTCGACGACC-3′). Samples were incubated for 10 min at 95 °C followed by 40 cycles of 95 °C for 15 s and 60 °C for 60 s in a Roche 480 LightCycler. Results were analysed by the comparative C_T ($\Delta\Delta C_T$) method and are presented as RNA levels relative to controls, as indicated.

FACS analysis. As previously described[37,47], single-cell suspensions of freshly excised tissues and/or capsules were prepared using a gentle MACS Dissociator (Miltenyi Biotec). Sample suspensions were prepared in passive PEB dissociation buffer (1X PBS pH 7.2, 2 mM EDTA and 0.5% BSA) and passed through 70 μm filters (cat. no. 22363548, Fisher Scientific) to remove debris. This procedure yielded the majority of cells adhered to implant surfaces (>90%). All tissue-derived samples were also subjected to red blood cell lysis with 5 ml of 1× RBC lysis buffer (cat. no. 00-4333, eBioscience) for 5 min at 4 °C, with termination through the addition of 20 ml sterile PBS. Remaining cells were centrifuged at 300–400 g and 4 °C and resuspended in 50 μl of staining buffer (cat. no. 00-4222, eBioscience) for staining in the dark for 25 min at 4 °C. Stains included monoclonal antibodies for CD11b (1 μl (0.2 μg) per sample; or CD11b–Alexa 488, clone M1/70, cat. no. 101217, BioLegend), LY6G (1 μl (0.5 μg) per sample; LY6G–Alexa 647, clone RB6-8C5, cat. no. 108418, BioLegend) and CD68 (1 μl (0.5 μg) per sample; CD68–Alexa 647, clone FA-11, cat. no. 11-5931, BioLegend). For FOXP3 T$_{reg}$ analyses, BioLegend antibodies for anti-mouse CD4 (1 μl (0.5 μg) per sample; CD4-Alexa 488, clone GK1.5, cat. no. 100425, BioLegend), CD25 (1 μl (0.2 μg) per sample; BV421-CD25, clone PC61, cat. no. 102043, BioLegend), anti-mouse, rat or human FOXP3 (5 μl (1 test) per sample; FOXP3–Alexa Fluor 647, clone 150D, cat. no. 320014, BioLegend); anti-α-SMA (1 μl per sample; α-SMA-Cy3, clone 1A4, cat. no. C6198, Sigma), and anti-FAP (1 μl per sample; FAP; clone 983802; cat. no. MAB9727, RnD Systems) used with 1 μl of subsequent secondary anti-rat Alexa Fluor 488 antibody (cat. no. A-11006, Thermo) following additional fixation with 1% paraformaldehyde and permeabilization with 0.1% Triton X-100. Two millilitres of flow cytometry stain buffer (cat. no. 00-4222, eBioscience) was then used for 3 consecutive wash steps involving centrifugation for 5 min (400–500 g at 4 °C), with supernatants aspirated between spins. Following all washes, samples were resuspended in 500 μl of flow cytometry staining buffer and run through a 40 μm filter (cat. no. 22363547, Fisher Scientific) for eventual FACS analysis using a BD LSRII or Fortessa (BD Biosciences). Unstained, single-antibody and IgG controls (labelled with either Alexa Fluor 488 or Alexa Fluor 647; BioLegend) were also used.

NanoString analysis. RNAs for mock (saline) controls or for various implant-bearing mice or rabbits ($n = 5$ per group) were isolated from described tissue samples at various time points after implantation. They were then quantified, diluted to the appropriate concentration (100 ng μl^{-1}), with 5 μl of each sample processed according to manufacturer protocols for analysis with our customized multiplexed gene panels. Rabbit RNAs were collected from samples retrieved over multiple months following implantation of various implants (described above) and analysed on a separate multiplexed rabbit gene-expression array. Expression levels were obtained following nCounter (NanoString Technologies) quantification, with samples analysed using nSolver analysis software (NanoString Technologies). Housekeeping genes *Cltc*, *Actb*, *Hprt1* and/or *Tubb5* were used to normalize the results, and data were log-transformed.

Statistical analysis. All line and bar graph data are expressed as mean ± s.e.m., with $n = 5$ mice per time point and per treatment group. Calculations regarding numbers of animals or individuals required for each experimental condition were determined via power analysis with G*Power software, assuming a normal distribution with alpha set to 0.05 assuming a normal distribution, and power set to 80%. Variance was estimated using previously published data[37,47] and other unpublished studies. In vivo experiments will be allotted 10% error for variation associated with any unplanned euthanasia. For example, to achieve significance in flow cytometric analysis of the immune microenvironment, we require $n = 5$ mice per condition as calculated by power analyses. All animals were included except in instances of unforeseen morbidity. Animal cohorts were also randomly selected. Blinding was used for these studies where possible (that is histology imaging, Nanostring, scRNA-seq, confocal imaging and all human sample analysis). In particular, human samples were de-identified before shipment to other parties for subsequent analysis, and they were only de-blinded once the data were collected. For rabbit studies, veterinary staff also had a separate log of which implants were in specific rabbit recipients; this list was also de-blinded upon subsequent analysis. Blinding, however, was not possible for in vitro analysis due to visual observations of implant surfaces. For FACS or qPCR, data were analysed for statistical significance by either one-way ANOVA with Bonferroni multiple-comparisons correction or unpaired, two-tailed t-test unless otherwise indicated, as implemented in GraphPad Prism 8. *$P < 0.05$, **$P < 0.001$ and ***$P < 0.0001$. High-throughput NanoString-based gene-expression data were normalized using the geometric means of the positive controls, with background levels established using the means of the negative controls. Data were then log-transformed. For each subtype, time and compartment group, a two-way ANOVA for the effect of size blocking on genes was performed. P-values were computed from pairwise comparisons performed using Tukey's honest significant difference test and the Bonferroni correction was used to control the overall error rate.

Reporting Summary. Further information on research design is available in the Nature Research Reporting Summary linked to this article.

Data availability

The main data supporting the findings of this study are available within the paper and its Supplementary Information. The raw and analysed datasets generated during the study are available for research purposes from the corresponding authors on reasonable request. High-throughput sequencing data have been deposited in the Gene Expression Omnibus (GEO) database, with series accession number GSE164645.

References

1. Teo, A. J. T. et al. Polymeric biomaterials for medical implants and devices. *ACS Biomater. Sci. Eng.* **2**, 454–472 (2016).
2. Lloyd, A. W., Faragher, R. G. & Denyer, S. P. Ocular biomaterials and implants. *Biomaterials* **22**, 769–785 (2001).
3. McLaughlin, K., Jones, B., Mactier, R. & Porteus, C. Long-term vascular access for hemodialysis using silicon dual-lumen catheters with guidewire replacement of catheters for technique salvage. *Am. J. Kidney Dis.* **29**, 553–559 (1997).
4. Khoo, C. T. Silicone synovitis. The current role of silicone elastomer implants in joint reconstruction. *J. Hand Surg. Br.* **18**, 679–686 (1993).
5. VandeVord, P. J. et al. Immune reactions associated with silicone-based ventriculo-peritoneal shunt malfunctions in children. *Biomaterials* **25**, 3853–3860 (2004).
6. Gabriel, A. & Maxwell, G. P. The evolution of breast implants. *Clin. Plast. Surg.* **42**, 399–404 (2015).
7. Yoda, R. Elastomers for biomedical applications. *J. Biomater. Sci. Polym. Ed.* **9**, 561–626 (1998).
8. Hanak, B. W., Bonow, R. H., Harris, C. A. & Browd, S. R. Cerebrospinal fluid shunting complications in children. *Pediatr. Neurosurg.* **52**, 381–400 (2017).
9. O'Malley, J. T., Burgess, B. J., Galler, D. & Nadol, J. B. Jr. Foreign body response to silicone in cochlear implant electrodes in the human. *Otol. Neurotol.* **38**, 970–977 (2017).
10. Coroneos, C. J. et al. US FDA breast implant postapproval studies: long-term outcomes in 99,993 patients. *Ann. Surg.* **269**, 30–36 (2019).
11. Headon, H., Kasem, A. & Mokbel, K. Capsular contracture after breast augmentation: an update for clinical practice. *Arch. Plast. Surg.* **42**, 532–543 (2015).

12. Castel, N., Soon-Sutton, T., Deptula, P., Flaherty, A. & Parsa, F. D. Polyurethane-coated breast implants revisited: a 30-year follow-up. *Arch. Plast. Surg.* **42**, 186–193 (2015).

13. Xu, H. et al. Hydrogel-coated ventricular catheters for high-risk patients receiving ventricular peritoneum shunt. *Medicine* **95**, e4252 (2016).

14. Barnea, Y., Hammond, D. C., Geffen, Y., Navon-Venezia, S. & Goldberg, K. Plasma activation of a breast implant shell in conjunction with antibacterial irrigants enhances antibacterial activity. *Aesthet. Surg. J.* **38**, 1188–1196 (2018).

15. Stevens, W. G. et al. Risk factor analysis for capsular contracture: a 5-year Sientra study analysis using round, smooth, and textured implants for breast augmentation. *Plast. Reconstr. Surg.* **132**, 1115–1123 (2013).

16. Mempin, M., Hu, H., Chowdhury, D., Deva, A. & Vickery, K. The A, B and C's of silicone breast implants: anaplastic large cell lymphoma, biofilm and capsular contracture. *Materials* **11**, 2393 (2018).

17. Mendonça, A. M., Santanelli di Pompeo, F. & De Mezerville, R. Nanotechnology, nanosurfaces and silicone gel breast implants: current aspects. *Case Rep. Plast. Surg. Hand Surg.* **4**, 99–113 (2017).

18. Munhoz, A. M., Clemens, M. W. & Nahabedian, M. Y. Breast implant surfaces and their impact on current practices: where we are now and where are we going. *Plast. Reconstr. Surg. Global Open* **7**, e2466 (2019).

19. Technical Committee ISO/TC 150. *ISO 14607 Non-Active Surgical Implants—Mammary Implants—Particular Requirements* 3rd edn (ISO copyright office, 2018).

20. Barnsley, G. P., Sigurdson, L. J. & Barnsley, S. E. Textured surface breast implants in the prevention of capsular contracture among breast augmentation patients: a meta-analysis of randomized controlled trials. *Plast. Reconstr. Surg.* **117**, 2182–2190 (2006).

21. Derby, B. M. & Codner, M. A. Textured silicone breast implant use in primary augmentation: core data update and review. *Plast. Reconstr. Surg.* **135**, 113–124 (2015).

22. Tevis, S. E. et al. Breast implant-associated anaplastic large cell lymphoma: a prospective series of 52 patients. *Ann. Surg.* https://doi.org/10.1097/SLA.0000000000004035 (2020).

23. Clemens, M. W. et al. Complete surgical excision is essential for the management of patients with breast implant-associated anaplastic large-cell lymphoma. *J. Clin. Oncol.* **34**, 160–168 (2016).

24. Kadin, M. E. et al. Biomarkers provide clues to early events in the pathogenesis of breast implant-associated anaplastic large cell lymphoma. *Aesthet. Surg. J.* **36**, 773–781 (2016).

25. Chung, L. et al. Interleukin-17 and senescent cells regulate the foreign body response to synthetic material implants in mice and humans. *Sci. Transl. Med.* https://doi.org/10.1126/scitranslmed.aax3799 (2020).

26. Loch-Wilkinson, A. et al. Breast implant-associated anaplastic large cell lymphoma in Australia and New Zealand: high-surface-area textured implants are associated with increased risk. *Plast. Reconstr. Surg.* **140**, 645–654 (2017).

27. Hallab, N. J., Samelko, L. & Hammond, D. The inflammatory effects of breast implant particulate shedding: comparison with orthopedic implants. *Aesthet. Surg. J.* **39**, S36–S48 (2019).

28. Parham, C. S. et al. Advising patients about breast implant associated anaplastic large cell lymphoma. *Gland Surg.* **10**, 417–442 (2020).

29. Hall-Findlay, E. J. Breast implant complication review: double capsules and late seromas. *Plast. Reconstr. Surg.* **127**, 56–66 (2011).

30. Wolfram, D. et al. T regulatory cells and T$_H$17 cells in peri-silicone implant capsular fibrosis. *Plast. Reconstr. Surg.* **129**, 327–337 (2012).

31. Chung, L. et al. Interleukin 17 and senescent cells regulate the foreign body response to synthetic material implants in mice and humans. *Sci. Transl. Med.* **12**, eaax3799 (2020).

32. Flemming, R. G., Murphy, C. J., Abrams, G. A., Goodman, S. L. & Nealey, P. F. Effects of synthetic micro- and nano-structured surfaces on cell behavior. *Biomaterials* **20**, 573–588 (1999).

33. Jain, N. & Vogel, V. Spatial confinement downsizes the inflammatory response of macrophages. *Nat. Mater.* **17**, 1134–1144 (2018).

34. Madden, L. R. et al. Proangiogenic scaffolds as functional templates for cardiac tissue engineering. *Proc. Natl Acad. Sci. USA* **107**, 15211–15216 (2010).

35. Kyle, D. J., Oikonomou, A., Hill, E. & Bayat, A. Development and functional evaluation of biomimetic silicone surfaces with hierarchical micro/nano-topographical features demonstrates favourable in vitro foreign body response of breast-derived fibroblasts. *Biomaterials* **52**, 88–102 (2015).

36. Sforza, M. et al. Preliminary 3-year evaluation of experience with SilkSurface and VelvetSurface Motiva silicone breast implants: a single-center experience with 5813 consecutive breast augmentation cases. *Aesthet. Surg. J.* **38**, S62–S73 (2018).

37. Doloff, J. C. et al. Colony stimulating factor-1 receptor is a central component of the foreign body response to biomaterial implants in rodents and non-human primates. *Nat. Mater.* **16**, 671–680 (2017).

38. Vegas, A. J. et al. Combinatorial hydrogel library enables identification of materials that mitigate the foreign body response in primates. *Nat. Biotechnol.* **34**, 345–352 (2016).

39. Veiseh, O. et al. Size- and shape-dependent foreign body immune response to materials implanted in rodents and non-human primates. *Nat. Mater.* **14**, 643–651 (2015).

40. Anderson, J. M., Rodriguez, A. & Chang, D. T. Foreign body reaction to biomaterials. *Semin. Immunol.* **20**, 86–100 (2008).

41. Kenneth Ward, W. A review of the foreign-body response to subcutaneously-implanted devices: the role of macrophages and cytokines in biofouling and fibrosis. *J. Diabetes Sci. Technol. Online* **2**, 768–777 (2008).

42. Bain, C. C. et al. Constant replenishment from circulating monocytes maintains the macrophage pool in the intestine of adult mice. *Nat. Immunol.* **15**, 929–937 (2014).

43. Abbas, A., Lichtman, A. & Pillai, S. in *Cellular and Molecular Immunology* 8th edn (Elsevier Saunders, 2014).

44. Efanov, J. I., Giot, J. P., Fernandez, J. & Danino, M. A. Breast-implant texturing associated with delamination of capsular layers: a histological analysis of the double capsule phenomenon. *Ann. Chir. Plast. Esthet.* **62**, 196–201 (2017).

45. Glicksman, C. A., Danino, M. A., Efanov, J. I., El Khatib, A. & Nelea, M. A step forward toward the understanding of the long-term pathogenesis of double capsule formation in macrotextured implants: a prospective histological analysis. *Aesthet. Surg. J.* **39**, 1191–1199 (2018).

46. Maxwell, G. P., Scheflan, M., Spear, S., Nava, M. B. & Heden, P. Benefits and limitations of macrotextured breast implants and consensus recommendations for optimizing their effectiveness. *Aesthet. Surg. J.* **34**, 876–881 (2014).

47. Farah, S. et al. Long-term implant fibrosis prevention in rodents and non-human primates using crystallized drug formulations. *Nat. Mater.* **18**, 892–904 (2019).

48. Cappellano, G. et al. Immunophenotypic characterization of human T cells after in vitro exposure to different silicone breast implant surfaces. *PLoS ONE* **13**, e0192108 (2018).

49. Katzin, W. E., Feng, L. J., Abbuhl, M. & Klein, M. A. Phenotype of lymphocytes associated with the inflammatory reaction to silicone gel breast implants. *Clin. Diagn. Lab Immunol.* **3**, 156–161 (1996).

50. Wynn, T. A. & Ramalingam, T. R. Mechanisms of fibrosis: therapeutic translation for fibrotic disease. *Nat. Med.* **18**, 1028–1040 (2012).

51. Sharabi, A. et al. Regulatory T cells in the treatment of disease. *Nat. Rev. Drug Discov.* **17**, 823–844 (2018).

52. Watad, A. et al. Silicone breast implants and the risk of autoimmune/rheumatic disorders: a real-world analysis. *Int J. Epidemiol.* **47**, 1846–1854 (2018).

53. Sadighi Akha, A. A. Aging and the immune system: an overview. *J. Immunol. Methods* **463**, 21–26 (2018).

54. Durbin, J. E., Hackenmiller, R., Simon, M. C. & Levy, D. E. Targeted disruption of the mouse Stat1 gene results in compromised innate immunity to viral disease. *Cell* **84**, 443–450 (1996).

55. O'Shea, J. J., Holland, S. M. & Staudt, L. M. JAKs and STATs in immunity, immunodeficiency, and cancer. *N. Engl. J. Med.* **368**, 161–170 (2013).

56. Liu, M. et al. CXCL10/IP-10 in infectious diseases pathogenesis and potential therapeutic implications. *Cytokine Growth Factor Rev.* **22**, 121–130 (2011).

57. Le Page, C., Genin, P., Baines, M. G. & Hiscott, J. Interferon activation and innate immunity. *Rev. Immunogenet.* **2**, 374–386 (2000).

58. Murray, P. J. et al. Macrophage activation and polarization: nomenclature and experimental guidelines. *Immunity* **41**, 14–20 (2014).

Acknowledgements

Author contributions

J.C.D., O.V. and R.L. designed the studies, analysed data and wrote the paper. J.C.D., O.V., M.S., J. Haupt, M.J., C.C., A.N., S.A.-F., J.L.S., S.J.B., S.Y.N., N.A.R., Y.E.H., I.M.L., H.C.H., R.N.M. and M.W.C. conducted the experiments. J.C.D., H.C.H. and O.V. carried out the statistical analyses and prepared displays communicating datasets. R.d.M., M.S., T.A.P., J. Hancock, A.M.M., A.B., B.M.K. and R.L. provided advice and technical support

throughout, and J.C.D., O.V. and R.L. contributed with supervision of the study. All authors discussed the results and the preparation of the paper.

Competing interests

J.H., A.B., B.K., T.A.P and R.L. are members of the Scientific Advisory Board of Establishment Labs Holdings and each hold equity in the company. M.S. and A.M.M. are members of the Medical Advisory Board and each hold equity in Establishment Labs Holdings. M.W.C. and B.M.K. are Investigators on the US IDE Clinical Trial for the Study of Safety and Effectiveness of Motiva Implants. R.D.M., N.A.R., Y.E.H. and I.M.L. are employees of Establishment Labs S.A., and hold equity in Establishment Labs Holdings. J.C.D. and O.V. are paid consultants for Establishment Labs S.A. For a list of entities with which R.L. is involved, compensated or uncompensated, see the listing in the Supplementary Information.

Additional information

Supplementary information The online version contains supplementary material available at https://doi.org/10.1038/s41551-021-00739-4.

Correspondence and requests for materials should be addressed to J.C.D., O.V., R.d.M. or R.L.

Peer review information *Nature Biomedical Engineering* thanks Pamela Moalli and the other, anonymous, reviewer(s) for their contribution to the peer review of this work.

Reprints and permissions information is available at www.nature.com/reprints.

Publisher's note Springer Nature remains neutral with regard to jurisdictional claims in published maps and institutional affiliations.

nature research

Corresponding author(s):	Joshua Doloff, Omid Veiseh, Roberto De Mezervilile, and Robert Langer
Last updated by author(s):	Apr 21, 2021

Reporting Summary

Nature Research wishes to improve the reproducibility of the work that we publish. This form provides structure for consistency and transparency in reporting. For further information on Nature Research policies, see our Editorial Policies and the Editorial Policy Checklist.

Statistics

For all statistical analyses, confirm that the following items are present in the figure legend, table legend, main text, or Methods section.

n/a	Confirmed	
☐	☒	The exact sample size (n) for each experimental group/condition, given as a discrete number and unit of measurement
☐	☒	A statement on whether measurements were taken from distinct samples or whether the same sample was measured repeatedly
☐	☒	The statistical test(s) used AND whether they are one- or two-sided *Only common tests should be described solely by name; describe more complex techniques in the Methods section.*
☒	☐	A description of all covariates tested
☐	☒	A description of any assumptions or corrections, such as tests of normality and adjustment for multiple comparisons
☐	☒	A full description of the statistical parameters including central tendency (e.g. means) or other basic estimates (e.g. regression coefficient) AND variation (e.g. standard deviation) or associated estimates of uncertainty (e.g. confidence intervals)
☐	☒	For null hypothesis testing, the test statistic (e.g. F, t, r) with confidence intervals, effect sizes, degrees of freedom and P value noted *Give P values as exact values whenever suitable.*
☒	☐	For Bayesian analysis, information on the choice of priors and Markov chain Monte Carlo settings
☒	☐	For hierarchical and complex designs, identification of the appropriate level for tests and full reporting of outcomes
☒	☐	Estimates of effect sizes (e.g. Cohen's d, Pearson's r), indicating how they were calculated

Our web collection on statistics for biologists contains articles on many of the points above.

Software and code

Policy information about availability of computer code

Data collection	All commercial software used is specified in Methods. No custom software code was used.
Data analysis	All commercial software used is specified in Methods. No custom software code was used.

For manuscripts utilizing custom algorithms or software that are central to the research but not yet described in published literature, software must be made available to editors and reviewers. We strongly encourage code deposition in a community repository (e.g. GitHub). See the Nature Research guidelines for submitting code & software for further information.

Data

Policy information about availability of data

All manuscripts must include a data availability statement. This statement should provide the following information, where applicable:
- Accession codes, unique identifiers, or web links for publicly available datasets
- A list of figures that have associated raw data
- A description of any restrictions on data availability

The main data supporting the findings of this study are available within the paper and its supplementary information. The raw and analysed datasets generated during the study are available for research purposes from the corresponding authors on reasonable request. High-throughput sequencing data have been deposited in the Gene Expression Omnibus (GEO) database, with series accession number GSE164645.

Field-specific reporting

Please select the one below that is the best fit for your research. If you are not sure, read the appropriate sections before making your selection.

☒ Life sciences ☐ Behavioural & social sciences ☐ Ecological, evolutionary & environmental sciences

For a reference copy of the document with all sections, see nature.com/documents/nr-reporting-summary-flat.pdf

Life sciences study design

All studies must disclose on these points even when the disclosure is negative.

Sample size	Calculations regarding the numbers of animals and individuals required for each experimental condition were determined via power analysis with the G*Power software. We assumed a normal distribution with alpha set to 0.05 and power set to 80%. In addition, we relied on journal guidelines for a minimum of n = 5 animals per treatment group, for all mouse, rabbit and human studies. The numbers are provided in the figure legends. We adhered to the sample-size requirements necessary for determining statistical significance.
Data exclusions	No data were excluded from analyses.
Replication	All attempts at replication were successful. Experimental repeat numbers are provided in the figure legends.
Randomization	Animal groups were randomized by body weight or age, and on the basis of when they were ordered and received.
Blinding	Blinding was used where possible (in histology imaging, Nanostring, single-cell RNA-seq, confocal imaging, and for all human-sample analysis). In particular, human samples were de-identified prior to shipment to other parties for subsequent analysis, and they were only unblinded once the data was collected. For the rabbit studies, veterinary staff also had a separate log of which implants were in which specific rabbit recipients; this list was also unblinded on subsequent analysis. Blinding, however, was not possible for in vitro analysis, owing to the visual observation of implant surfaces.

Reporting for specific materials, systems and methods

We require information from authors about some types of materials, experimental systems and methods used in many studies. Here, indicate whether each material, system or method listed is relevant to your study. If you are not sure if a list item applies to your research, read the appropriate section before selecting a response.

Materials & experimental systems

n/a	Involved in the study
☐	☒ Antibodies
☒	☐ Eukaryotic cell lines
☒	☐ Palaeontology and archaeology
☐	☒ Animals and other organisms
☐	☒ Human research participants
☒	☐ Clinical data
☒	☐ Dual use research of concern

Methods

n/a	Involved in the study
☒	☐ ChIP-seq
☐	☒ Flow cytometry
☒	☐ MRI-based neuroimaging

Antibodies

Antibodies used	Stains included monoclonal antibodies for CD11b (1 ul (0.2 ug) per sample; or CD11b-Alexa-488, Clone M1/70, Catalog number: 101217, BioLegend), Ly-6G (Gr-1) (1 ul (0.5 ug) per sample; Ly-6G-Alexa-647, Clone RB6-8C5, Catalog number:108418, BioLegend), and CD68 (1 ul (0.5 ug) per sample; CD68-Alexa647, Clone FA-11, Catalog number:11-5931, BioLegend). For FoxP3-Treg analyses, BioLegend antibodies for anti-mouse CD4 (1 ul (0.5 ug) per sample; CD4-Alexa488, Clone GK1.5, Catalog number: 100425, BioLegend), CD25 (1 ul (0.2 ug) per sample; BV421-CD25, Clone PC61, Catalog number: 102043, BioLegend), anti-mouse/rat/human FoxP3 (5 ul (1 test) per sample; FoxP3-Alexa647, Clone 150D, Catalog number: 320014, BioLegend); anti-Alpha-Smooth Muscle actin (1 ul per sample; Alpha-SMact-Cy3, Clone 1A4, Catalog number: C6198, Sigma), and anti-Fibroblast activation protein (1 ul per sample; FAP; Clone 983802; Catalog number: MAB9727, RnD Systems) used with 1 ul of subsequent secondary anti-rat AlexaFluor-488 (Catalog number: A-11006, Thermo) were employed. Dilutions are all specified for this application at 1:200.
Validation	As previously described in refs. 38 and 48, for macrophage and neutrophil antibody stains, additional validation information can be found on the BioLegend website as well as in our Supplementary Fig. 15 for T-cell antibody staining and for T-cell and Treg identification. We have also added flow-cytometry data in Supplementary Figs. 17 and 21.

Animals and other organisms

Policy information about [studies involving animals](#); [ARRIVE guidelines](#) recommended for reporting animal research

Laboratory animals	Immune-competent 8-week-old female C57BL/6 mice (Jackson Laboratory, Bar Harbor, ME), and female 3–4 kg New Zealand White Rabbits (Charles River, Wilmington, MA).
Wild animals	The study did not involve wild animals.
Field-collected samples	The samples did not involve samples collected from the field.
Ethics oversight	All animal surgeries and protocols were carried out in complete compliance with all relevant ethical regulations, as approved by the MIT Committee on Animal Care, (IACUC). All surgical procedures as well as the post-operative care were supervised by the veterinary staff of the MIT Division of Comparative Medicine.

Note that full information on the approval of the study protocol must also be provided in the manuscript.

Human research participants

Policy information about [studies involving human research participants](#)

Population characteristics	Details on patient information are provided in Supplementary Table 4.
Recruitment	No active recruitment needed. All samples were sourced from previously collected tissue banks.
Ethics oversight	De-identified clinical specimens of capsules were harvested from patients. Smooth (Allergan) or Biocell (Allergan) were collected following institutional review board approval at MD Anderson Cancer Center, after acquisition of informed consent from the patients. Similarly, capsule tissue from patients receiving SmoothSilk breast implants (Establishment Labs) were obtained from the Establishment Labs tissue bank, which collected specimens, as determined by the Scientific Ethical Committee of the Costa Rican Institute for Research and Teaching in Nutrition and Health Foundation.

Note that full information on the approval of the study protocol must also be provided in the manuscript.

Flow Cytometry

Plots

Confirm that:

☒ The axis labels state the marker and fluorochrome used (e.g. CD4-FITC).

☒ The axis scales are clearly visible. Include numbers along axes only for bottom left plot of group (a 'group' is an analysis of identical markers).

☒ All plots are contour plots with outliers or pseudocolor plots.

☒ A numerical value for number of cells or percentage (with statistics) is provided.

Methodology

Sample preparation	To obtain single-cell suspensions, we used methodology previously optimized and published in Doloff et al., 2017 and 2019 (refs. 38 and 48).
Instrument	FACS analysis was carried out by using a BD LSRII or Fortessa (BD Biosciences, San Jose, CA, USA).
Software	FloJo.
Cell population abundance	Sorting was not done. However, for FACS gating analysis: cell populations of interest (such as macrophages) were incredibly abundant as main responders to material implant systems, reaching as much as 50% to 70% of the dissociated tissue or fibrotic capsule on implant surfaces. With that said, percentages and abundance (cell numbers) decreased significantly due to the inclusion of some implant groups, as reflected in figures in the paper. We also report the analysis of T-cell abundance, and although not as prevalent as macrophage populations (by %), they were repeatably observed and statistically significant over background.
Gating strategy	The macrophage-gating strategy was the same as previously optimized and published in Doloff et al., 2017 and 2019 Nature Materials (refs. 38 and 48). Therefore, all flow-cytometry data in this study are shown exclusively as quantified bar graphs with error bars reflecting data spread, along with symbols reflecting the degree of statistical significance. Figures exemplifying the gating strategy were provided in refs. 38 and 48. A new Treg-gating strategy widely used in the literature and employing CD3, CD4, CD25, and FoxP3 positive status (BioLegend website) is provided in Supplementary Fig. 15.

☒ Tick this box to confirm that a figure exemplifying the gating strategy is provided in the Supplementary Information.